Toward Physics-Based Nonergodic PSHA: A Prototype Fully Deterministic Seismic Hazard Model for Southern California

Kevin R. Milner*[1], Bruce E. Shaw[2], Christine A. Goulet[1], Keith B. Richards-Dinger[3], Scott Callaghan[1], Thomas H. Jordan[4], James H. Dieterich[3], and Edward H. Field[5]

ABSTRACT

We present a nonergodic framework for probabilistic seismic-hazard analysis (PSHA) that is constructed entirely of deterministic, physical models. The use of deterministic ground-motion simulations in PSHA calculations is not new (e.g., CyberShake), but prior studies relied on kinematic rupture generators to extend empirical earthquake rupture forecasts. Fully dynamic models, which simulate rupture nucleation and propagation of static and dynamic stresses, are still computationally intractable for the large simulation domains and many seismic cycles required to perform PSHA. Instead, we employ the Rate-State earthquake simulator (RSQSim) to efficiently simulate hundreds of thousands of years of M ≥ 6.5 earthquake sequences on the California fault system. RSQSim produces full slip-time histories for each rupture, which, unlike kinematic models, emerge from frictional properties, fault geometry, and stress transfer; all intrinsic variability is deterministic. We use these slip-time histories directly as input to a 3D wave-propagation code within the CyberShake platform to obtain simulated $F_{max} = 0.5$ Hz ground motions. The resulting 3 s spectral acceleration ground motions closely match empirical ground-motion model (GMM) estimates of median and variability of shaking. When computed over a range of sources and sites, the variability is similar to that of ergodic GMMs. Variability is reduced for individual pairs of sources and sites that repeatedly sample a single path, which is expected for a nonergodic model. This results in increased exceedance probabilities for certain characteristic ground motions for a source–site pair, while decreasing probabilities at the extreme tails of the ergodic GMM predictions. We present these comparisons and preliminary fully deterministic physics-based RSQSim–CyberShake hazard curves, as well as a new technique for estimating within- and between-event variability through simulation.

KEY POINTS

- Estimates of seismic hazards are often controlled by large variability terms in ergodic ground-motion models.
- We develop a physics-based nonergodic framework to characterize repeatable source and path effects.
- This approach reduces design-level hazard for many sites by removing blanket ergodic uncertainty.

Supplemental Material

INTRODUCTION

Probabilistic seismic-hazard analysis (PSHA), first formalized by Cornell (1968), is typically performed by combining an earthquake rupture forecast (ERF) with a set of empirical ground-motion models (GMMs) to estimate the probability of exceeding various shaking intensity measures (gray pathway in Fig. 1). ERFs have traditionally relied on observed fault slip rates, scaling relationships, and regional magnitude–frequency distributions to estimate the rate of large earthquakes on predefined fault segments (e.g., Field *et al.*, 2014). Empirical GMMs are developed through regression of recorded ground motions, using equations that are consistent with the basic physical phenomena of source scaling, wave propagation, and site effects, but are uncertain. The recorded ground-motion datasets used to constrain GMMs are rapidly expanding but remain particularly

1. University of Southern California, Southern California Earthquake Center, Los Angeles, California, U.S.A.; 2. Lamont-Doherty Earth Observatory, Columbia University, Palisades, New York, U.S.A.; 3. University of California, Riverside, Riverside, California, U.S.A.; 4. University of Southern California, Los Angeles, California, U.S.A.; 5. Geologic Hazards Science Center, U.S. Geological Survey, Golden, Colorado, U.S.A.

*Corresponding author: kmilner@usc.edu

Cite this article as Milner, K. R., B. E. Shaw, C. A. Goulet, K. B. Richards-Dinger, S. Callaghan, T. H. Jordan, J. H. Dieterich, and E. H. Field (2021). Toward Physics-Based Nonergodic PSHA: A Prototype Fully Deterministic Seismic Hazard Model for Southern California, *Bull. Seismol. Soc. Am.* **111**, 898–915, doi: 10.1785/0120200216

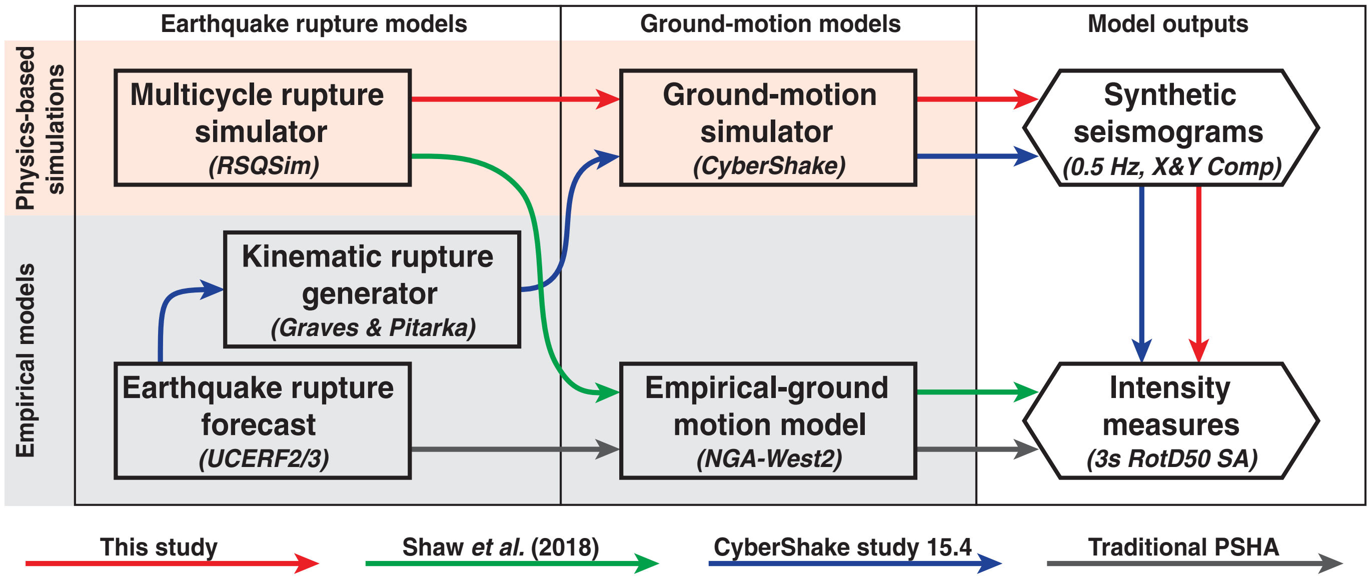

sparse for two types of events that pose the greatest risk to human life and infrastructure: large, complex ruptures, and those at short site–rupture distances. This paucity of data gives rise to epistemic uncertainties that can be slowly reduced as rare events occur in well-instrumented regions. In addition, GMM developers typically employ the ergodic assumption, which asserts that the distribution of ground-motion recordings across many sites and ruptures can be used to describe the expected shaking for any single site–rupture pair, and manifests as scatter about median predictions. For a given ergodic GMM, that scatter is modeled as a large aleatory variability term, which Anderson and Brune (1999) noted controls hazard at long return periods (Fig. 2), and is, by definition, irreducible under the ergodic assumption. However, components of this GMM variability can be reduced using physical models of fault rupture and seismic-wave propagation. These physical models are imperfect, but their uncertainties are epistemic and can, therefore, potentially be reduced as knowledge is gained.

We present results from one set of physical models (red pathway in Fig. 1) to demonstrate how nonergodic, physics-based PSHA can reduce design-level ground motions at many sites by quantifying repeated path, source, and site effects. This reduction is nonuniform, and the models can also identify areas likely to exceed ergodic predictions. Prior physics-based PSHA studies have relied on statistically based earthquake rupture forecasts (ERFs) (blue pathway in Fig. 1), for example, Graves *et al.* (2011) and Jordan *et al.* (2018). Other studies have performed fully dynamic multicycle rupture simulations (e.g., Galvez *et al.*, 2019) of hundreds to thousands of years of seismicity on single faults or small regions. Here, we present an end-to-end, physics-based PSHA approach, considering hundreds of thousands of years of synthetic seismicity on a large and complex fault system. First, we compare total ground-motion variance to that from an ergodic GMM and examine the variance structure using a new simulation-based technique

Figure 1. Probabilistic seismic-hazard analysis (PSHA) pathways. This study presents a new pathway, shown with red arrows, which combines a multicycle earthquake rupture simulator directly with a ground-motion simulator to compute synthetic seismograms. Shaw *et al.* (2018), shown with green arrows, combined a multicycle earthquake rupture simulator with an empirical ground-motion model (GMM). Prior CyberShake studies, shown with blue arrows, used a kinematic rupture generator to extend an empirical earthquake rupture forecast (ERF) for ground-motion simulation. Traditional PSHA studies, shown with gray arrows, combine an empirical ERF with empirical GMMs.

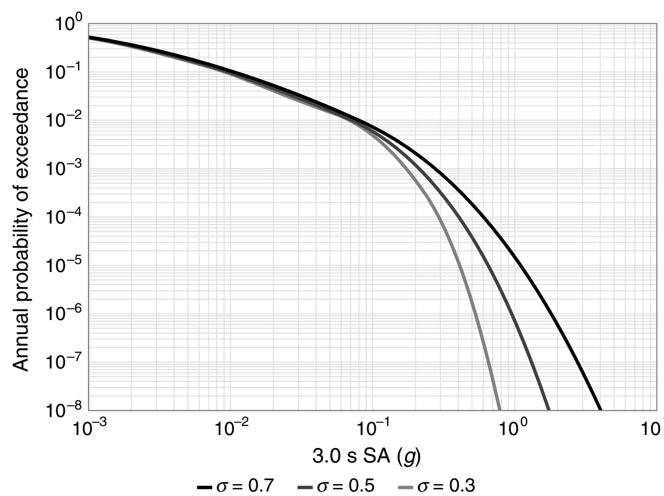

Figure 2. Ground-motion variability controls hazard at large intensities (e.g., $>0.2g$). This example is computed for the University of Southern California (USC) site with the Third Uniform California Earthquake Rupture Forecast (UCERF3) model and Abrahamson *et al.* (2014; henceforth ASK2014) GMM, modified with three different fixed total sigma values for illustration purposes. A typical GMM total sigma value of 0.7 is plotted in black, and reduced values of 0.5 and 0.3 are plotted in gray and light gray, respectively. As sigma decreases, which may be possible with nonergodic modeling, the probability of exceeding the largest ground motions, for example, $>1g$ 3 s spectral acceleration (SA), decreases dramatically.

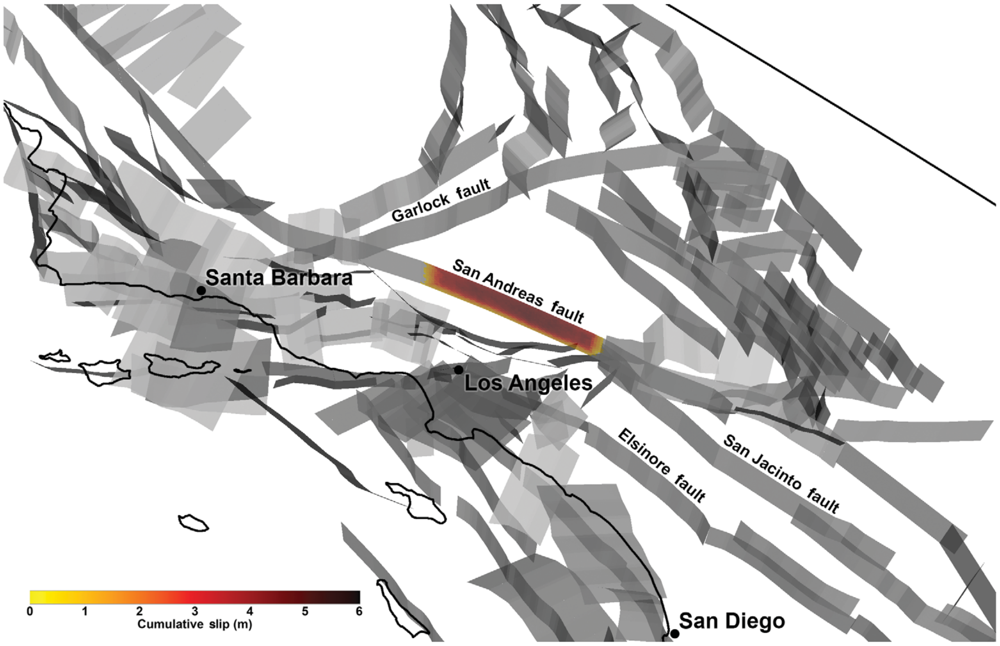

Figure 3. 3D perspective view looking north of faults considered in southern California, highlighting an **M** 7.5 simulated Rate-State earthquake simulator (RSQSim) rupture on the Mojave section of the San Andreas fault. Darker colors represent higher patches of total cumulative slip, and major faults and cities are annotated. All other fault patches that did not participate in the rupture are shown in gray.

developed to estimate within- and between-event variability. Then, we compute hazard curves for sites in the Los Angeles region and contrast them with those from a traditional ergodic approach.

Extensive validation against available data and a robust accounting of epistemic uncertainties are required before use for engineering design, and additional computational and scientific advances are required before these techniques are applicable to short spectral periods. Specifically, this study focuses on 3 s spectral accelerations from 0.5 Hz ground-motion simulations of $\mathbf{M} \geq 6.5$ ruptures using a single synthetic catalog, but we hope that it will encourage further development of these and other candidate physical PSHA models and illustrate their potential utility.

SOURCE MODEL: RATE-STATE EARTHQUAKE SIMULATOR (RSQSim)

We replace traditional ERFs with the RSQSim, a multicycle physics-based earthquake simulator developed by Dieterich and Richards-Dinger (2010). Shaw *et al.* (2018) found that RSQSim simulations, using the fault system developed as part of the Third Uniform California Earthquake Rupture Forecast (UCERF3; Field *et al.*, 2014), produce seismicity catalogs that match long-term UCERF3 rates on major faults, and are largely indistinguishable from the UCERF3 rate model when carried through empirical GMM-based PSHA calculations (green pathway in Fig. 1). RSQSim is computationally efficient, owing to numerous analytic approximations and a boundary-element, event-driven, three-state algorithm; this allows it to generate long synthetic catalogs (hundreds of thousands of years) of seismicity on the complex California fault system (Richards-Dinger and Dieterich, 2012). Rupture nucleation and propagation in RSQSim is governed by rate- and state-dependent friction (Dieterich, 1992). In states 0 (healing) and 1 (nucleating slip), RSQSim employs a quasi-static approximation that balances the shear stress applied to each fault patch by the frictional shear stress. During state 2 (earthquake slip), RSQSim uses a first-order quasidynamic approximation, with a stepwise constant sliding speed and dynamic overshoot. Unlike traditional ERFs, RSQSim produces full slip-time histories for all simulated ruptures, which can be used directly as input to deterministic wave-propagation simulations. Rupture stress drops (see supplemental material available to this article), hypocenters, and roughness are fully deterministic and dependent only on global frictional parameters and the state of stress at nucleation. Figure 3 shows the cumulative slip of an **M** 7.5 rupture on the Mojave section of the San Andreas fault embedded in the fault model for southern California, and Figure 4 shows a side view of the same rupture, including its time evolution. RSQSim catalogs of seismicity include many complex multifault ruptures consistent with recent observations (e.g., the 2016 **M** 7.8 Kaikoura earthquake) and the UCERF3 model. Figure 5 shows one such particularly complex multifault rupture, an **M** 7.8 that nucleates on the Compton fault before spreading to the Newport–Inglewood, Palos Verdes, and seven other UCERF3 fault sections.

For this study, we use a synthetic catalog simulated on the full statewide UCERF3 fault system with the hybrid-loading approach discussed in Shaw (2019), discretized into 265,464 individual triangular fault patches, each with an average area of 1.35 km^2. This catalog incorporates three RSQSim improvements implemented since Shaw *et al.* (2018), each of which is aimed to improve rupture propagation velocity (v_{prop}) and rupture ground motions: finite receiver patch geometry, variable slip speed, and static-elastic time delay. Figure 6 shows mean v_{prop} as a function of patch hypocentral distance (R_{hyp}) for each

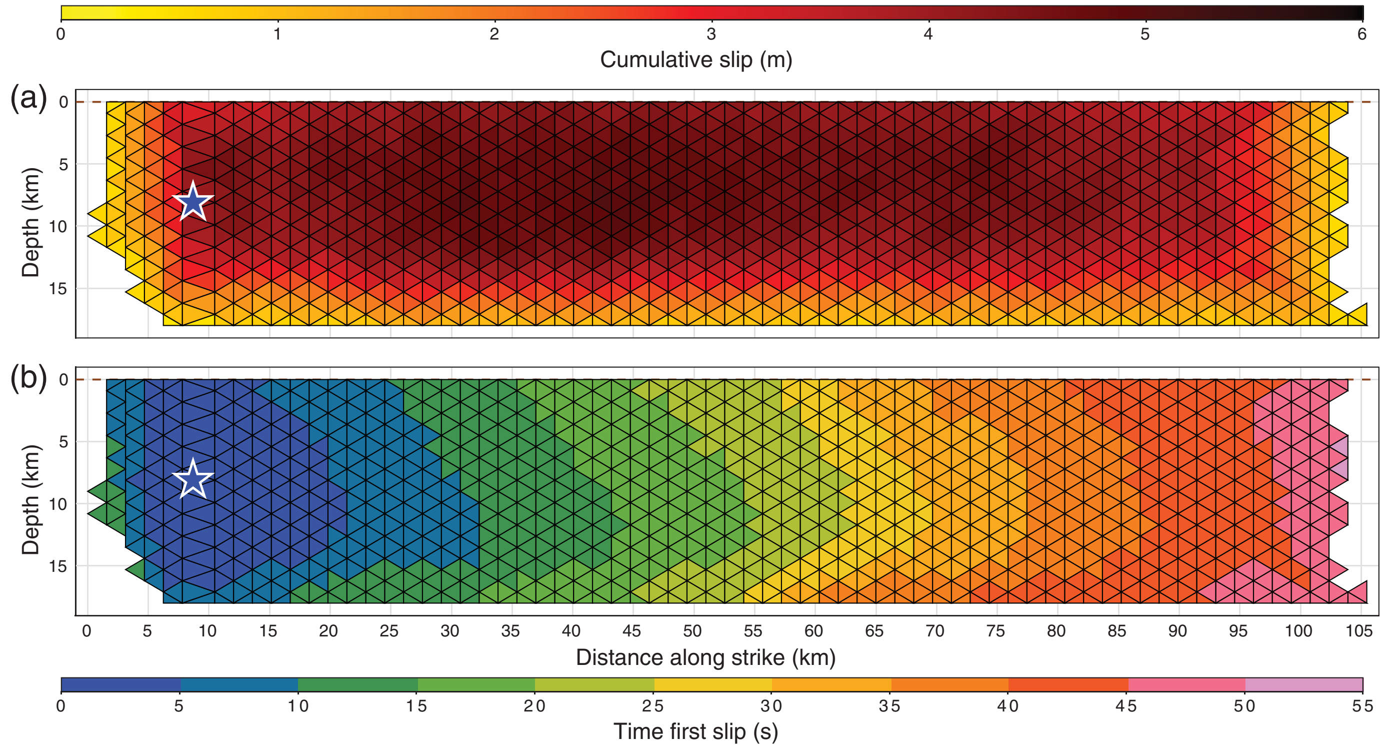

Figure 4. 2D side view of the **M** 7.5 simulated RSQSim rupture from Figure 3. The common x axis is the along-strike distance of the rupture in kilometers, with zero at the southeast end of the rupture and the maximum at the northwest end. The y axis of each panel is the depth of each triangular RSQSim patch from the free surface. (a) Total cumulative slip with darker colors indicating areas of greater slip. (b) Plots the time from rupture nucleation (in seconds) that each patch first slipped, contoured in 5 s intervals. The rupture hypocenter is noted with a star.

model iteration. Mean propagation velocities for the catalog used by Shaw *et al.* (2018) are $v_{\mathrm{prop}} \in [0.9, 1.6]$ km/s for $R_{\mathrm{hyp}} > 10$ km (dashed line in Fig. 6). This is significantly lower than typical values of $v_{\mathrm{prop}} \in [2.1, 2.4]$ km/s, if we assume a shear-wave velocity of $\beta = 3$ km/s and the relations established in Andrews (1976) and Geller (1976) of $v_{\mathrm{prop}} \in [0.7\beta, 0.8\beta]$. This propagation velocity deficit resulted in low along-strike forward rupture directivity in numerical ground-motion simulations (rupture directivity comparisons are discussed in the supplemental material).

The first RSQSim modification improves the accuracy of the stiffness matrices, K^{τ} and K^{σ} for shear and normal stresses, respectively. Previously, this calculation considered the finite geometry of the source patch that slips, but employed a single-point representation of the receiving patch. Now, the calculated stiffness is averaged over the finite geometry of the receiver patch. This results in increased $v_{\mathrm{prop}} \in [1.5, 2.25]$ km/s for $R_{\mathrm{hyp}} > 10$ km and greatly increased v_{prop} of patches neighboring the hypocenter to supershear speeds on average, in this case, $v_{\mathrm{prop}} = 4.4$ km/s for $R_{\mathrm{hyp}} \simeq 1$ km (dotted line in Fig. 6). These changes in v_{prop} increase ground motions in aggregate, but the deficit of along-strike forward directivity with this model is still apparent.

The second modification eliminates the fixed sliding speed approximation during earthquake slip (state 2). That slip velocity is determined by the shear impedance relationship (Brune, 1970),

$$v_{\mathrm{eq}} = \frac{2\beta\Delta\tau}{G}, \tag{1}$$

in which $\Delta\tau$ is the difference between the shear stress at initiation of slip and sliding friction, and G is the shear modulus. In Shaw *et al.* (2018), that value was estimated a priori for all patches using typical values of $\Delta\tau$, with a uniform $v_{\mathrm{eq}} = 1$ m/s. Here, we introduce a variable slip speed version of RSQSim, in which v_{eq} for each patch is set according to equation (1) from $\Delta\tau$ at the moment it enters state 2, and then updated stepwise during a slip episode. This stepwise discretization is necessitated by the efficient state-driven RSQSim computational scheme, which cannot accommodate continuously variable v_{eq}. Updates occur whenever the instantaneous calculated velocity leaves the range $[v_{\mathrm{eq}} \times \xi, v_{\mathrm{eq}}/\xi]$, in which $\xi \in (0, 1)$ is a dimensionless constant and $\xi = 0.8$ in this study. A velocity floor is also applied as a multiplicative factor of the initially calculated slip speed in each slip episode (0.3 for this study). Figure 7 shows the slip-time evolution on a single patch, with seven slip episodes from the rupture depicted in Figures 3 and 4. The multiple slip episodes in Figure 7 are, in part, due to the velocity floor, that is, the second episode can be viewed as a continuation of the first with a reset lower floor; without such a floor, all of the slip would have possibly

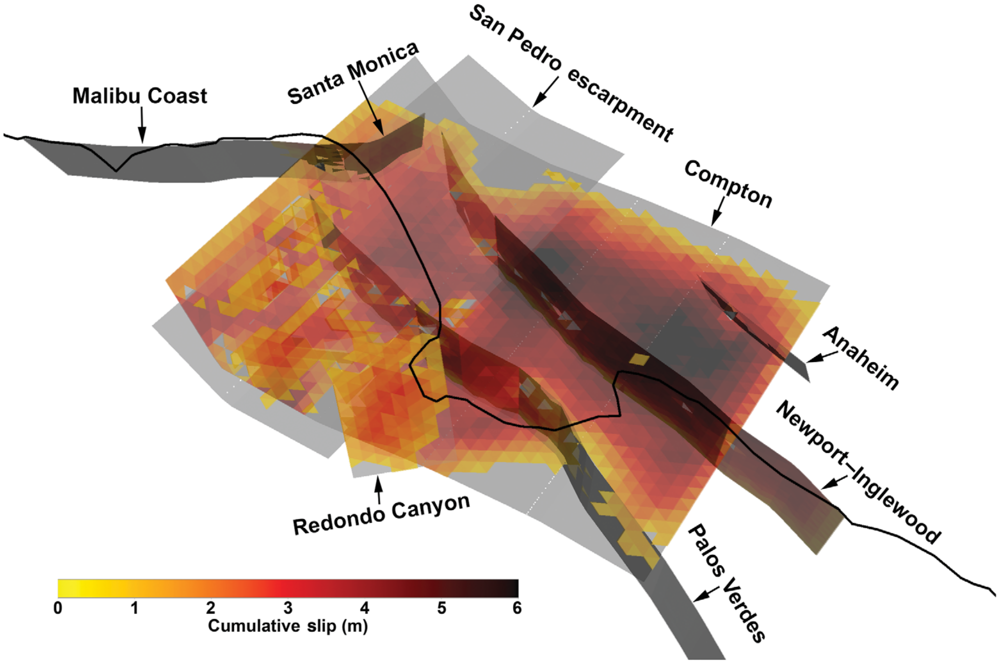

Figure 5. 3D perspective view looking north of a complex synthetic **M** 7.8 RSQSim rupture in the Los Angeles basin. It nucleates on the Compton fault and then spreads to the Newport–Inglewood, Palos Verdes, and other nearby faults. In total, 10 different UCERF3 fault sections participate, but the three previously named account for greater than 90% of the total seismic moment. Darker colors represent higher patches of total cumulative slip, and participating faults are labeled (Elysian Park and San Pedro basin also participate but are omitted as their contributions to the total seismic moment released are negligible).

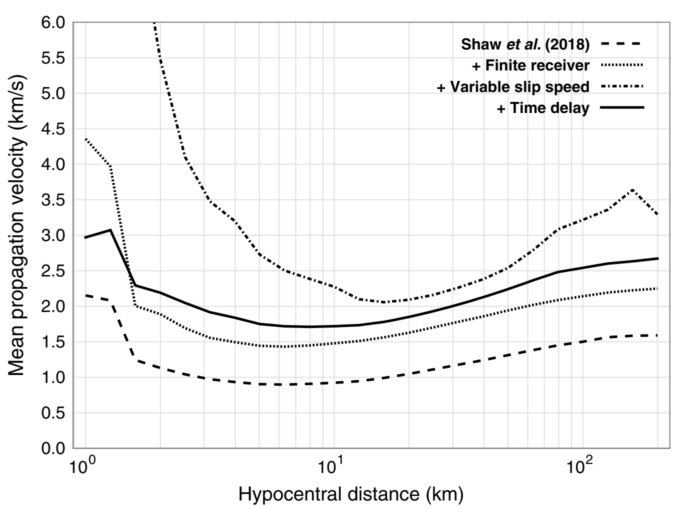

Figure 6. Propagation velocity as a function of patch hypocentral distance for four different RSQSim parameterizations, each of which incorporates a new feature over the previous model. The base model is the catalog used in Shaw *et al.* (2018), plotted with a dashed line. The first modification, plotted with a dotted line, adds a new finite receiver patch capability to the stiffness matrix calculations. The second modification, plotted with a dotted and dashed line, adds variable slip speed capabilities to RSQSim, with stepwise updating of sliding velocity on a patch during earthquake slip. The final model, plotted with a solid line and used for PSHA calculations in this study, also includes a time delay to the static-elastic interaction.

been accommodated by one long crack-like episode. Values of ξ and the velocity floor were determined through trial and error, to maintain computational efficiency while generating reasonable ground motions. Future work will examine the details of these and other model choices on RSQSim slip-time histories and ground motions in more detail. Variable slip speed models exhibit greatly increased propagation velocities, with mean $v_{\mathrm{prop}} \in [2, 4]$ km/s for $R_{\mathrm{hyp}} > 10$ km and highly unphysical values, up to $v_{\mathrm{prop}} = 17.5$ km/s, for $R_{\mathrm{hyp}} \simeq 1$ km (dotted and dashed line in Fig. 6).

Our third modification reduces these unphysical initial rupture velocities by adding a time delay to the static elastic interaction. Without this delay, all stress changes are felt instantaneously on all patches in RSQSim. Ideally, the stress change experienced on the ith patch, due to slip on the jth patch, would be delayed by $\Delta t_{\mathrm{causal}}(i, j) = \frac{d(i,j)}{\beta}$, in which $d(i, j)$ is the distance between the centers of the two patches. This would necessitate a unique time delay for each source and receiver patch pair, breaking the RSQSim paradigm of fixed state-driven updates. Instead, we simplify this to a single fixed-time delay applied for all $i \neq j$, tuned to roughly match the expected delay for each patch's immediate neighbors (because it is those interactions that control the rupture velocity). We calculate this time delay from the patch's shear self-stiffness, $K^{\tau}(j, j)$, valid if neighboring elements are of similar size and shape:

$$\Delta t_{\mathrm{causal}}(i, j) = \frac{\eta G}{\beta |K^{\tau}(j, j)|}, \qquad (2)$$

in which η is a tuneable dimensionless constant. We use value of $\eta = 0.67$, chosen through trial and error, to obtain reasonable average propagation velocities, resulting in values for our final model in the range $v_{\mathrm{prop}} \in [1.5, 3]$ km/s for all R_{hyp} (solid line in Fig. 6).

The total synthetic catalog length is 714,516 yr after throwing out model spin-up time at the beginning of the catalog; we chose a conservative value of 65,000 yr of spin-up time, which ensures that the faults in the study region with the lowest slip rates participated in at least one event prior to the final catalog start time and most participated in many. We consider a total of

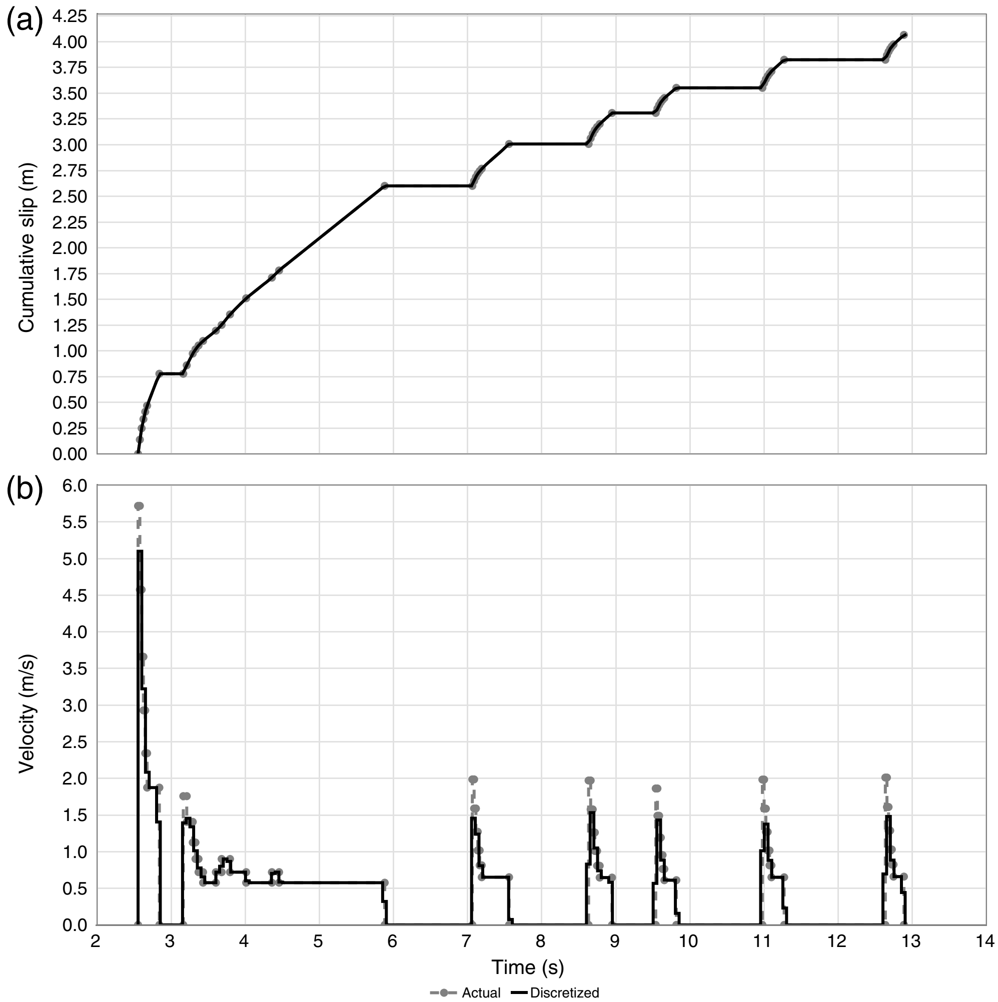

Figure 7. Slip-time history of a single patch from the rupture depicted in Figures 3 and 4. (a) Cumulative slip and (b) instantaneous velocity, both as a function of time from rupture nucleation. The actual slip-time history of the patch from the RSQSim transitions file, which alternates between locked, slipping, and slip speed updates, is plotted as gray dashed lines with circles at each transition point. Black lines show a discretized (at 0.1 s) slip-time history, which adjusts velocities to preserve total displacement (used as input to CyberShake).

220,927 ruptures with $\mathbf{M} \geq 6.5$. Considerable runtime is required to generate catalogs that are sufficiently long for robust PSHA calculations; it took eight days of wall-clock time on 64 Frontera compute nodes (3584 processors) at the Texas Advanced Computing Center to generate this catalog. Model output includes the time at which each triangular fault patch transitions between states (i.e., starts or stops sliding, or updates sliding velocity), which we convert to the standard rupture format (SRF; see Data and Resources) source description for use as input to our wave-propagation codes. The SRF description requires that slip velocity for each patch be evenly discretized in time; we achieve this by computing the total displacement that occurred during each SRF timestep and then setting the velocity as that displacement divided by the timestep duration. This ensures that the total displacement (and thus seismic moment released) is preserved for each rupture but results in timesteps in which the velocity differs from that in the RSQSim model output, smoothing out short-lived velocity peaks. Figure 7 shows the slip-time history for a single patch, before (gray lines) and after (black lines) this adjustment.

GMM: CyberShake

The CyberShake platform (Graves *et al.*, 2011; Jordan *et al.*, 2018) replaces empirical GMMs with deterministic 3D ground-motion simulations through 3D seismic velocity models, characterizing the effects of basin response and other path effects that are either parameterized or treated as aleatory variability in empirical GMMs. In prior studies, CyberShake has relied on traditional ERFs to define rupture properties (magnitude, geometry, and probability) and a stochastic kinematic rupture generator (Graves and Pitarka, 2014) to produce a suite of slip-time histories for each rupture with prescribed rupture properties (blue pathway in Fig. 1). Ground-motion variability in CyberShake has previously been represented through ensembles of rupture variations, which vary the hypocenter location and kinematic slip distributions of each input ERF rupture, as well as aleatory magnitude variability for a given source area to produce ruptures with a variety of stress drops. The process of automated kinematic rupture generation is currently limited to contiguous planar or ribbon-like faults, which has restricted CyberShake to the older UCERF2 (Field *et al.*, 2009) model that lacks multifault ruptures. As such, previous CyberShake studies do not represent complex multifault ruptures such as the one depicted in Figure 5, which are also prevalent in the UCERF3 model.

For this study, we instead couple the RSQSim model with CyberShake, to create the first PSHA model for a complex fault system composed entirely of fully deterministic physical models. We use the Southern California Earthquake Center (SCEC) CVM-S4.26.M01 tomographically inverted velocity model with geotechnical layer (Lee *et al.*, 2014; Small *et al.*, 2017),

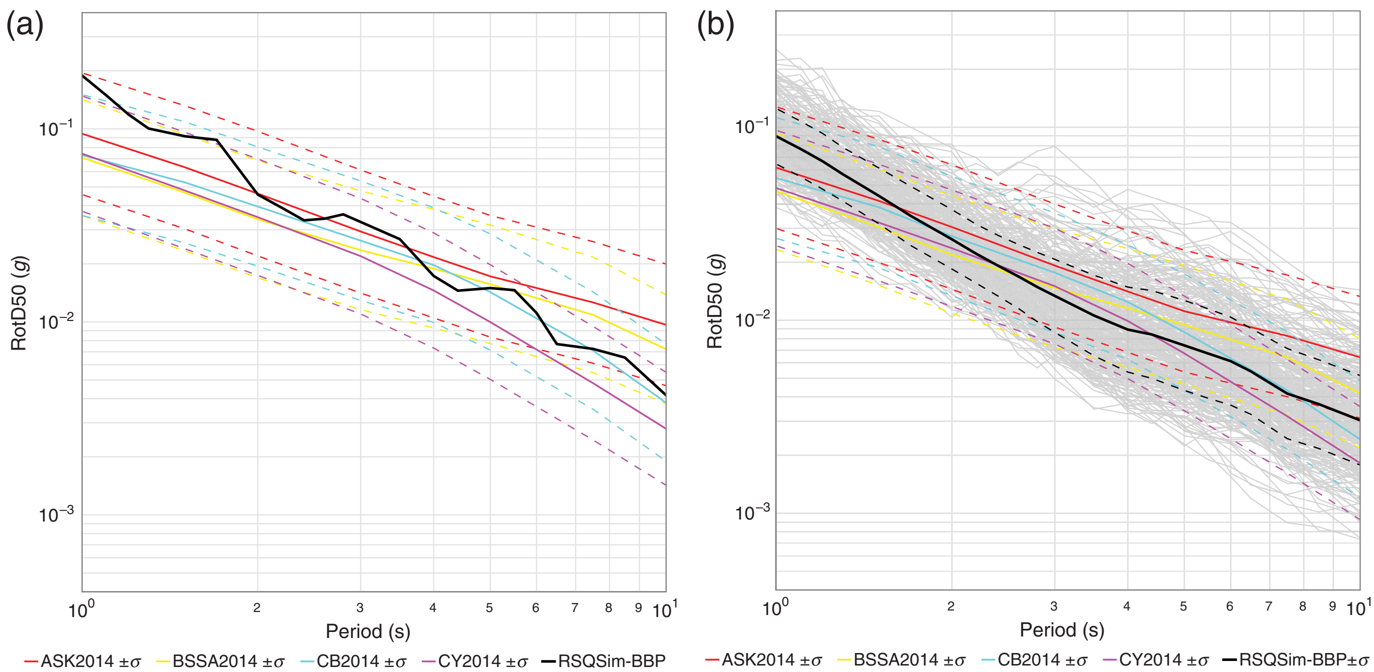

to perform 0.5 Hz simulations for the entire RSQSim catalog for a set of 10 sites in the Los Angeles region. We consider 3 s RotD50 (Boore, 2010) 5% damped pseudospectral accelerations (PSAs), which are the shortest spectral period that can be reliably represented by CyberShake 0.5 Hz simulations. CyberShake utilizes seismic reciprocity (Zhao *et al.*, 2006) to efficiently compute synthetic seismograms from hundreds of thousands of sources at a single site through just two 3D strain Green tensor simulations (one for each horizontal component of resultant seismograms). This efficiency makes simulation of all ruptures within 200 km of a site from our 714,516 yr RSQSim catalog tractable on modern supercomputers.

Figure 8. RotD50 spectra for site USC from ruptures on the Mojave section of the San Andreas fault, computed with a 1D velocity structure with $V_{S30} =$ 500 m/s in the Southern California Earthquake Center (SCEC) Broadband Platform (BBP). (a) Spectrum for the **M** 7.5 rupture on the Mojave section of the San Andreas fault in Figures 3 and 4, plotted as a thick black line. (b) Spectra for 321 different 7.0 ≤ **M** ≤ 7.5 RSQSim ruptures on the Mojave section of the San Andreas fault simulated at USC plotted with thin gray lines, the mean of all 321 ruptures as a thick black line, and the mean ±1 standard deviation with dashed black lines. GMM comparisons (with ±1 standard deviation bounds marked with dashed lines) are plotted with colored lines. GMM predictions are slightly different for panel (b), because distributions are averaged across those predicted for each of the 321 RSQSim ruptures (rather than for a single **M** 7.5 rupture in panel (a)). BSSA2014, Boore *et al.* (2014); CB2014, Campbell and Bozorgnia (2014); CY2014, Chiou and Youngs (2014).

GROUND-MOTION VARIABILITY IN 1D: SCEC BROADBAND PLATFORM

We initially prototyped this calculation with 3D simulations in a 1D layered earth structure in the SCEC Broadband Platform (BBP), version 19.4.0 (Maechling *et al.*, 2014), calculating RotD50 spectra ($T \in [1, 10]$ s) for each RSQSim rupture at a number of sites in Los Angeles. We used the Los Angeles basin velocity model with $V_{S30} = 500$ m/s and the deterministic low-frequency component of the Graves and Pitarka (2016) simulation method, to simulate ground motions for RSQSim slip-time histories in the SRF representation; this calculation was done at 4 Hz and low-pass filtered at 2 Hz (as opposed to 0.5 Hz for the CyberShake calculations presented later). Figure 8a plots spectra computed for a site at the University of Southern California (USC) for a single **M** 7.5 rupture on the Mojave section of the San Andreas fault calculated with the BBP and compared with four empirical GMMs from the enhancement of Next Generation Attenuation Relationships for western US project (henceforth NGA-West2; Abrahamson *et al.*, 2014; Boore *et al.*, 2014; Bozorgnia *et al.* 2014; Campbell and Bozorgnia, 2014; Chiou and Youngs, 2014). GMM comparisons with BBP are parameterized with the same $V_{S30} = 500$ m/s site condition, and basin depth is set according to the 1D velocity profile: $Z_{1.0} = 0.2$ km or $Z_{2.5} = 2.5$ km, depending on the model. We use the methodology described in Shaw *et al.* (2018) to parameterize RSQSim ruptures for empirical GMM estimation, first mapping the arbitrarily complex RSQSim ruptures to their corresponding UCERF3 fault subsections. This mapping step is included to correct rupture–site distances (R_{Rup} and R_{JB}) for complex ruptures, which may include one or more patches from faults other than the main rupture surface that might be close to the site of interest but not significantly contribute to the ground motion at that site. In that case, distances are instead calculated to the nearest UCERF3 fault subsection surface in which at least 20% of the subsection (by area) participates in the RSQSim rupture.

Although no individual rupture is expected to match any given mean GMM spectra exactly, the distribution of spectra from all similar ruptures (Fig. 8b) can be statistically compared with GMMs. In aggregate, 1D BBP results for this fault simulated at site USC are similar to and within the uncertainties of GMM predictions, although, the variability is less than predicted by ergodic GMMs. We plot a histogram of simulated amplitudes for a single spectral period of 3 s in Figure 9a, compared with empirical GMM predicted lognormal distributions. Here, reduced variability of the 1D BBP results is more apparent (especially at the tails of the GMM distributions). The lower variability, however, is expected when contrasting simulations of a single seismic source, repeatedly sampling the same path from source to site (here in a 1D layered velocity structure) and with the same rupture incidence angle, with ergodic GMMs.

Expanding this analysis to 10 sites (listed in supplemental material and mapped in Fig. 10) and across all RSQSim ruptures within 200 km of each site in our catalog, we turn to the z-score statistical measure to explore total variability of RSQSim simulated ground motions. The z-score, $z(i,j)$, computes the logarithmic difference between the ground-motion intensity of the ith rupture simulated at the jth site, $Y_{\mathrm{sim}}(i,j)$, and the GMM-predicted intensity, $Y_{\mathrm{GMM}}(i,j)$, in units of total GMM standard deviation, $\sigma_{\mathrm{GMM}}(i,j)$:

$$z(i,j) = \frac{\ln Y_{\mathrm{sim}}(i,j) - \langle \ln Y_{\mathrm{GMM}}(i,j) \rangle}{\sigma_{\mathrm{GMM}}(i,j)}. \tag{3}$$

This statistic allows us to compare the variability of RSQSim–BBP ground motions with those predicted by GMMs, to quantify bias and to compare the total variability across many site locations, magnitudes, and distances. A histogram of z-scores from all RSQSim–BBP simulations compared with the Abrahamson *et al.* (2014; henceforth ASK2014) GMM is plotted as a gray histogram in Figure 11a. The mean of −0.01 (in units of σ_{GMM}) indicates that this RSQSim–BBP model has no significant bias relative to the ASK2014 GMM. The narrower distribution of the z-score histogram (relative to the standard normal plotted as a black line) with a fractional standard deviation (σ-fract) of 0.61 illustrates the lower variability from 1D RSQSim–BBP relative to the ASK2014 GMM. This is expected with a 1D velocity structure lacking basin structures and heterogeneities that focus and scatter seismic energy. We focus on comparisons with a single GMM (ASK2014) from here on, but mean z-scores are similar using the other NGA-West2 relations: 0.24 with Boore *et al.* (2014), −0.04 with Campbell and Bozorgnia (2014), and 0.12 with Chiou and Youngs (2014).

GROUND-MOTION VARIABILITY IN 3D: CyberShake

We next performed full 3D deterministic simulations using the SCEC CyberShake platform. Heterogeneities in the CVM-S4.26.M01 velocity model enhance the ground-motion

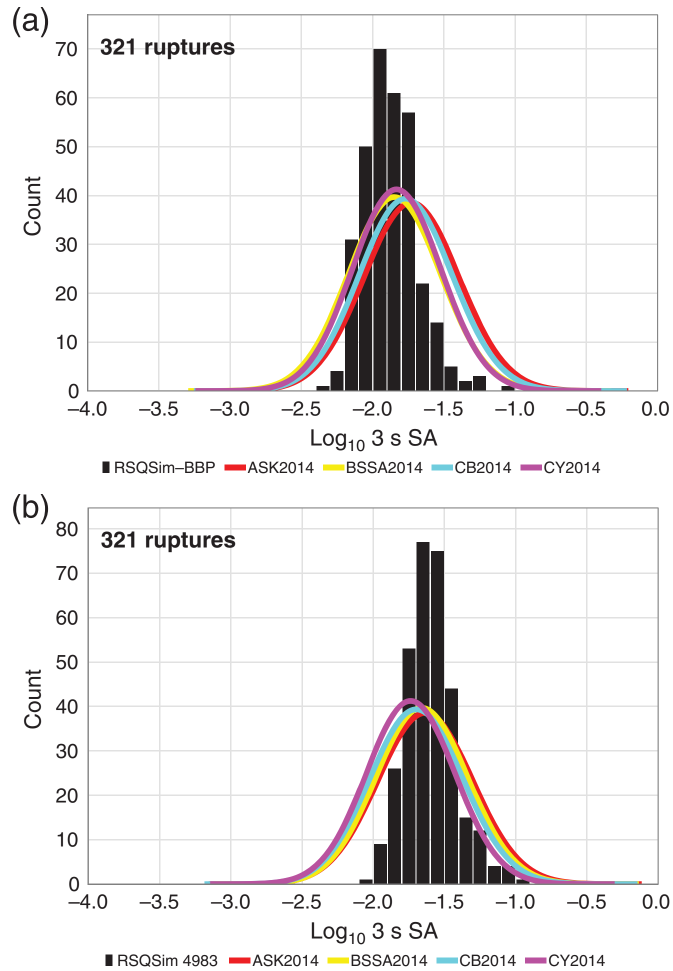

Figure 9. All 7 ≤ **M** ≤ 7.5 San Andreas (Mojave) RSQSim events (black histogram) for a site at USC, 3-s RotD50 ground-motion histograms of accelerations. (a) 1D velocity structure in the SCEC BBP. (b) 3D velocity structure for a site at USC. GMM predicted lognormal distributions are plotted with colored lines.

variability relative to the 1D case, and deep sedimentary basins tend to amplify the shaking. The z-score histograms computed with CyberShake for the same set of sites and ruptures as before (Fig. 11b) illustrate this increased variability, along with larger mean intensities than those from both the GMM and BBP. Each CyberShake site was set to have a surface V_S of 500 m/s, which we consider equivalent to the $V_{S30} = 500$ m/s site condition in the ASK2014 GMM, because the mesh gridpoint spacing in 0.5 Hz CyberShake calculations is larger than 30 m. We set the $Z_{1.0}$ basin depth proxy value in ASK2014 from the CVM-S4.26.M01 velocity model, with values listed in the supplemental material. The mean z-score increases to 0.57, meaning that RSQSim–CyberShake 3 s RotD50 ground motions are on average 0.57 ASK2014 standard deviations above the mean ASK2014 prediction, and the σ-fract of 0.77 indicates that the RSQSim–CyberShake model for these 10 sites contains 77% of the total variability in ASK2014. The z-score histograms

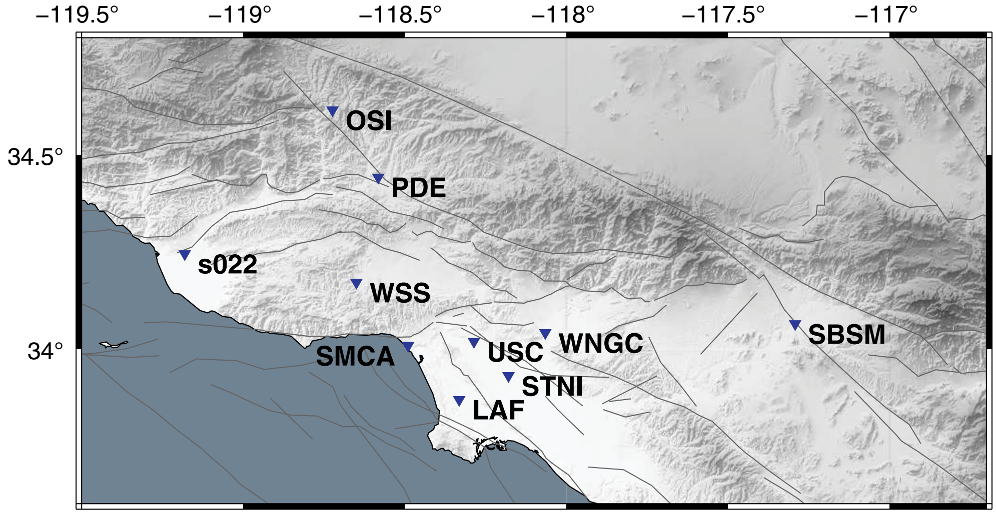

Figure 10. Map view of sites considered in this study, with site locations marked with triangles next to their names. Site locations are listed in the supplemental material. Fault traces from UCERF3 are drawn with thin gray lines. The color version of this figure is available only in the electronic edition.

The z-score histogram of Figure 11b is convenient in that it summarizes variability across many sites, magnitudes, and distances, but it can hide model trade-offs and biases. To illustrate this, consider two alternative candidate models: one ergodic that matches the empirical GMM median and total standard deviation perfectly across all unique combinations of explanatory variable values (e.g., magnitude and distance), and another nonergodic of which the standard deviation is smaller than the empirical GMM for each unique combination and mean residuals (relative to the empirical GMM) are sampled from a normal distribution. Both models could have identical z-score histograms (with zero mean), even with very different variance structures. This scenario is depicted in Figure 12, with a cartoon of z-scores from an ergodic model in Figure 12a and a nonergodic model with the sum of many narrow distributions in Figure 12b. We must thus decompose the model variance to verify that its individual components are in line with GMM predictions, not only its total variance.

Al Atik *et al.* (2010) explained how empirical GMMs typically decompose total variance into two sources, both zero mean and independent normally distributed random variables: between-event (denoted δB with standard deviation τ) and within-event (denoted δW with standard deviation ϕ). The variables τ and ϕ are typically estimated through mixed-effects regression (Abrahamson and Youngs, 1992; Al Atik and Abrahamson, 2010), which accounts for irregularly sized and sparse datasets. Wang and Jordan (2014) demonstrated an averaging-based factorization approach to estimate τ and ϕ for simulation-based PSHA using a prior southern California CyberShake study, although, their methodology is best suited for larger datasets (they used 235 CyberShake sites).

We developed a technique to estimate τ and ϕ_{ss} from RSQSim ruptures using a smaller set of $N_{site} = 10$ CyberShake sites, all chosen with the same approximate soil classification (in this case modeled surface $V_s = 500$ m/s) and distributed throughout southern California (Fig. 10). We compute the single-site within-event standard deviation, ϕ_{ss}, rather than full ϕ, because our model does not contain unexplained site-to-site variance. Instead of performing hundreds of computationally expensive forward ground-motion simulations for individual RSQSim ruptures to estimate τ and ϕ_{ss}, we take advantage of the seismic reciprocity assumption employed in CyberShake

for each individual site are given in the supplemental material. The bias toward higher ground motions for soft-soil and basin sites has been observed in previous CyberShake studies (Jordan *et al.*, 2018). In this case, the bias in RSQSim–CyberShake is lower than in the CyberShake Study 15.4 that used the UCERF2 ERF extended with the Graves and Pitarka (2014) kinematic rupture generator. The z-scores from Study 15.4 are plotted in Figure 11c, with a mean z-score of 1.00 for this same set of 10 sites, and a similar amount of total variability (σ-fract of 0.85) to the RSQSim–CyberShake model. Both Study 15.4, and this study used the same 3D velocity model and deterministic ground-motion simulation code (Cui *et al.*, 2013), so the additional z-score bias seen in Study 15.4 is due to differences in the source models themselves, such as stress drop and propagation velocities. Further comparisons between RSQSim and the Graves and Pitarka (2014, 2016) rupture generators are warranted but are outside the scope of this study.

For the single source–site pair of San Andreas Mojave with $7 \le \mathbf{M} \le 7.5$ ruptures simulated at USC (Fig. 9b), variability remains lower than the ergodic GMM prediction, although, for this site, the distribution shifts to the right due to deeper soft soils in the CVM-S4.26.M01 model at this site than in the 1D BBP model plotted in Figure 9a. This is expected due to the repeated sampling of a single path, this time through a 3D medium, from the same source to the USC site.

PROCEDURE TO DECOMPOSE VARIANCE THROUGH ROTATION AND TRANSLATION

Figure 11b indicates that RSQSim–CyberShake ground motions contain a similar (though slightly lower) amount of total variability as empirical GMMs, but that alone is not sufficient to validate the variance structure of the model.

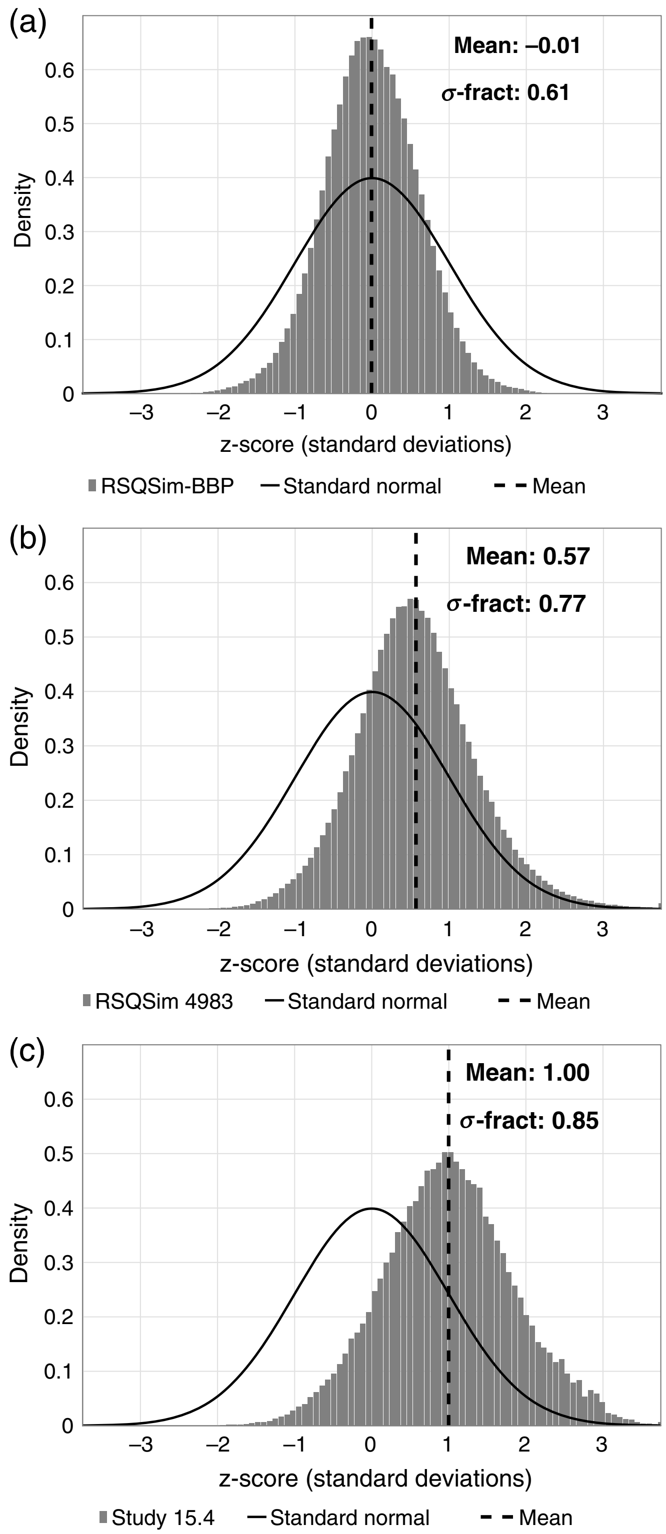

Figure 11. The z-score (equation 3) distributions (gray histograms) of all ruptures for the sites from Figure 10, compared against the ASK2014 GMM. A standard normal distribution is overlaid with a black line, and the mean z-score value is indicated with a thick dashed vertical line. (a) RSQSim rupture ground motions simulated with BBP and a 1D velocity structure. (b) RSQSim rupture ground motions simulated with the SCEC CyberShake platform and a 3D velocity structure. (c) UCERF2 ruptures extended with the Graves and Pitarka (2014) kinematic rupture generator simulated with the SCEC CyberShake platform (Study 15.4).

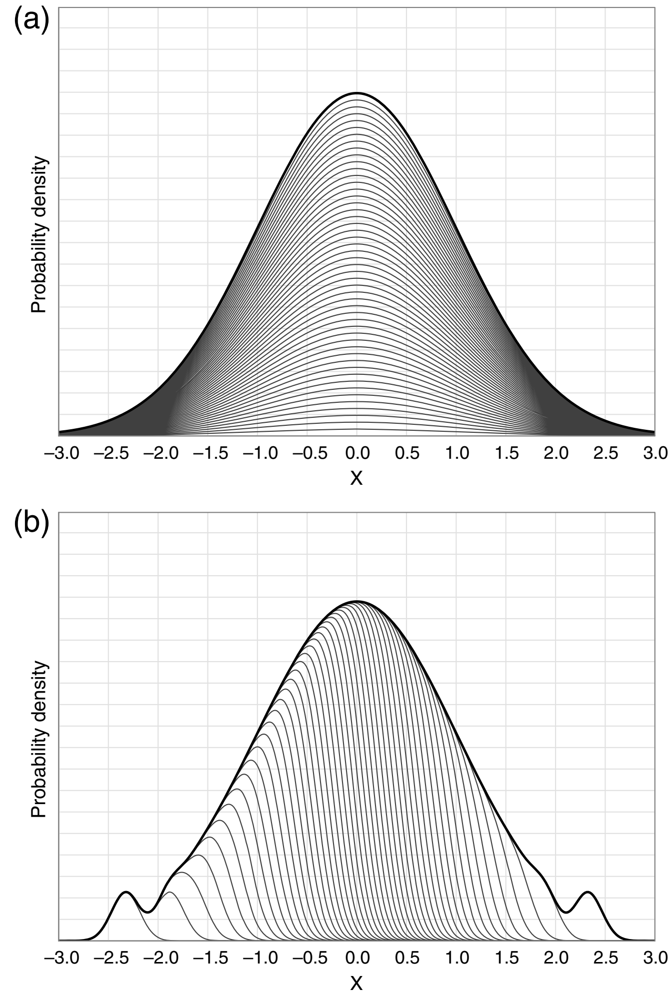

Figure 12. Stacked normal distributions, with the total sum represented with a thick black line and the cumulative sum after each of $N = 50$ individual distributions with thin gray lines. (a) The sum in which each distribution is a standard normal, and (b) in which the mean values are uniformly sampled from a standard normal and the standard deviation given by $\sigma = \sqrt{\frac{1}{N}}$. As N approaches infinity, the sum of all distributions in panel (b) is normally distributed and matches that from panel (a).

by rotating and translating ruptures around each CyberShake site. This allows us to mimic an ergodic sample by performing only two CyberShake Green's function simulations (one for each horizontal component) at each site (Zhao *et al.*, 2006). We recover ground motions sampling hundreds of thousands of different combinations of ruptures, rupture orientations, paths, and distances. The simulation scheme we are about to describe is summarized in Figure 13 and defines a scenario as a type of earthquake with explicitly enumerated criteria (e.g., **M** 6.6 strike slip), a rupture as a unique event (slip-time history, magnitude, and geographic extent), which occurred in the RSQSim simulation, and a rotated rupture as a modified rupture slip-time history that has been rotated and translated horizontally in space. We first selected three sets of $N_{\mathrm{rup}} = 50$ unique ruptures, which satisfy the criteria for the following scenarios:

1. **M** 6.6 vertical strike slip: $\mathbf{M} \in [6.55, 6.65]$, $z_{\mathrm{TOR}} \in [0, 1]$, rake $\in \{-180, 0, 180\}$, dip $= 90$, linear (maximum 0.5 km deviation from ideal linear source).
2. **M** 6.6 reverse: $\mathbf{M} \in [6.55, 6.65]$, $z_{\mathrm{TOR}} \in [1, 5]$, rake $\in [80, 100]$, dip $\in [35, 55]$.
3. **M** 7.2 vertical strike slip: $\mathbf{M} \in [7.15, 7.25]$, $z_{\mathrm{TOR}} \in [0, 1]$, rake $\in \{-180, 0, 180\}$, dip $= 90$, linear (maximum 5% deviation from ideal linear source).

More than 50 candidate ruptures exist for each scenario; we narrowed the set down to $N_{\mathrm{rup}} = 50$ ruptures for each scenario by choosing a random set that minimizes the number of repeat ruptures on individual fault sections. This results in ruptures from a diverse set of sources, with 51, 20, and 66 different fault sections participating in ruptures for scenarios 1, 2, and 3, respectively. The counts for scenarios 1 and 3 are greater than N_{rup}, because multiple sections can participate in a single rupture. The two **M** 6.6 scenarios were selected to approximate the larger-magnitude scenarios proposed in the Goulet *et al.* (2014) BBP "Part B" validation exercise, which were, in turn, chosen due to an abundance of data at those magnitudes to constrain empirical GMMs. We consider $N_{\mathrm{dist}} = 3$ fixed 3D distances (R_{Rup}) between each rupture and site: {20,50,100} km (the first two distances were also taken from the BBP "Part B" exercise). First, we rotate and translate each rupture such that its scalar moment centroid is due north of our site, its strike is zero (due north, following the Aki and Richards, 2009, convention), and the minimum distance between the site and the rotated rupture is as prescribed. We repeat this for a total of $N_{\mathrm{az}} = 18$ different strike azimuths (each 20° apart) to capture variability due to rupture directivity and geometric effects. This is done by first rotating each rupture in place about its centroid, then translating the rotated rupture toward or away from the site to correct for any changes to R_{Rup} as a result of this rotation. We repeat this procedure sampling $N_{\mathrm{path}} = 18$ different paths from the site to the rotated rupture (each 20° apart), rotating the rupture about the site in addition to rotating the rupture in place for each path. This procedure is more clearly illustrated through a schematic with just five rupture strike azimuth and path rotations each in Figure 13. We simulate the ground motions in CyberShake for each unique combination of rupture i, site j, distance k, strike azimuth l, and path m, for scenario n, $Y_{\mathrm{sim}}(i, j, k, l, m, n)$. Weighting of irregularly sampled data is a primary motivation for the mixed-effects regression technique employed in empirical studies; we avoid this by prescribing the same number of simulations for each unique RSQSim rupture, $N_{\mathrm{az}} \times N_{\mathrm{path}} = 324$, with a total of $N_{\mathrm{az}} \times N_{\mathrm{path}} \times N_{\mathrm{dist}} \times N_{\mathrm{rup}} = 48{,}600$ simulated ground motions for each scenario computed at a single site.

We estimate τ and ϕ_{ss} separately for each scenario n, $\tau(n)$, and $\phi_{\mathrm{ss}}(n)$. Values are reported in Table 1 for τ and Table 2 for ϕ_{ss}, including each individual distance to test distance dependence, the range of distance-independent values across each site, and also total site- and distance-independent τ and ϕ_{ss}. First, we compute the event term (natural-log median ground motion) for each rupture simulated at site j,

$$B(i,j,k,n) = \mathrm{mdn.}\{\ln(Y_{\mathrm{sim}}(i,j,k,l,m,n)) | l \in 1..N_{\mathrm{az}}, m \in 1..N_{\mathrm{path}}\}. \quad (4)$$

This is analogous to δB_e in Al Atik *et al.* (2010), except that here it is computed for a single site at a fixed distance (but still sampling many paths and rupture orientations, because of the experiment design) and not expressed as a residual relative to an empirical model (we are after the variability component only). We take the between-event standard deviation computed for site j, for ruptures matching scenario n, and at a fixed distance k, to be the standard deviation of the set of all $B(i, j, k, n)$,

$$\tau(j, k, n) = \mathrm{st.dev.}\{B(i, j, k, n) | i \in 1..N_{\mathrm{rup}}\}. \quad (5)$$

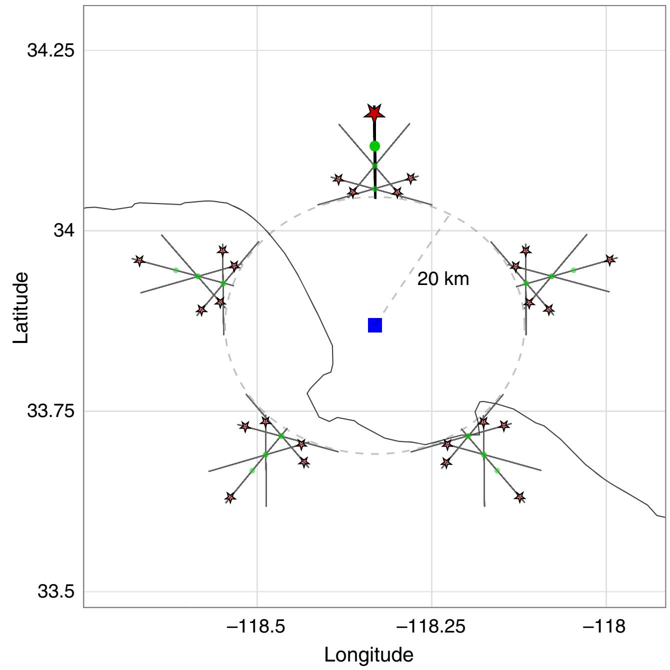

Figure 13. Map view schematic plot of rupture rotation and translation procedure to emulate empirical records within CyberShake's reciprocity framework. This schematic includes just five source and path azimuths each, for clarity, as opposed to 18 each used for the calculation. The surface of the initial rotated rupture, in this case one that matches the **M** 6.6 vertical strike-slip scenario, is depicted with a thick black line, its epicenter a large star, and its scalar moment centroid a large circle. Each rotated rupture is initially translated such that it is a fixed distance (in this case $R_{\mathrm{Rup}} = 20$ km, annotated with a dashed circle) due north of the site (site USC in this example, depicted as a square in the center of the map). The rotated rupture is then rotated multiple times, both in place about its centroid and about the site, holding R_{Rup} constant. These additional rotated rupture surfaces are depicted with thin gray lines, their epicenters small stars, and their scalar moment centroids small circles. The Los Angeles coastline is drawn in black at the bottom left of the map. The color version of this figure is available only in the electronic edition.

TABLE 1
Between-Event Standard Deviations

Scenario	Simulated $\tau(n)$	Range of $\tau(j,n)$	$\tau(k,n)$, $k=20$ km	$\tau(k,n)$, $k=50$ km	$\tau(k,n)$, $k=100$ km
M 6.6, vertical strike slip	0.18	[0.16, 0.23]	0.19	0.19	0.17
M 6.6, reverse	0.17	[0.16, 0.26]	0.17	0.18	0.17
M 7.2, vertical strike slip	0.14	[0.13, 0.16]	0.14	0.14	0.13

Between-event standard deviations for 3 s spectral acceleration (SA) estimated for scenarios defined in the Procedure to Decompose Variance Through Rotation and Translation section. Columns include the total simulated between-event standard deviations, $\tau(n)$ (equation 9), the range of simulated $\tau(j,n)$ from each site (equation 6), and values for individual distances computed across all sites, $\tau(k,n)$ (equation 8).

TABLE 2
Within-Event Standard Deviations

Scenario	Simulated $\phi_{ss}(n)$	Range of $\phi_{ss}(j,n)$	$\phi_{ss}(k,n)$, $k=20$ km	$\phi_{ss}(k,n)$, $k=50$ km	$\phi_{ss}(k,n)$, $k=100$ km
M 6.6, vertical strike slip	0.48	[0.38, 0.64]	0.43	0.48	0.52
M 6.6, reverse	0.44	[0.37, 0.56]	0.39	0.45	0.48
M 7.2, vertical strike slip	0.44	[0.35, 0.60]	0.39	0.45	0.48

Within-event standard deviations for 3 s spectral acceleration (SA) estimated for scenarios defined in the Procedure to Decompose Variance Through Rotation and Translation section. Columns include the total simulated within-event standard deviations, $\phi_{ss}(n)$ (equation 14), the range of simulated $\phi_{ss}(j,n)$ from each site (equation 12), and values for individual distances computed across all sites, $\phi_{ss}(k,n)$ (equation 13).

ASK2014 and the other of the NGA-West2 relations outlined in Bozorgnia *et al.* (2014) assume distance independence of τ for 3 s RotD50 (which is consistent with our results), so we compute distance independent $\tau(j,n)$ as the mean of $\tau(j,k,n)$ across all distances,

$$\tau(j,n) = \langle\{\tau(j,k,n)|k \in 1..N_{\text{dist}}\}\rangle. \quad (6)$$

We extend this to multiple sites by computing event terms across all sites, again ensuring that each site has the same approximate soil classification (in this case, surface $V_s = 500$ m/s for all sites),

$$B(i,k,n) = mdn.\{ln(Y_{\text{sim}}(i,j,k,l,m,n))|j \in 1..N_{\text{site}}, \times l \in 1..N_{\text{az}}, m \in 1..N_{\text{path}}\}. \quad (7)$$

Similar to equations (5) and (6), we take the between-event standard deviation across all sites for scenario n at distance k as the standard deviation of the set of all $B(i,k,n)$,

$$\tau(k,n) = \text{st.dev.}\{B(i,k,n)|i \in 1..N_{\text{rup}}\}, \quad (8)$$

and the total between-event standard deviation for all ruptures matching scenario n as the mean of all $\tau(j,k,n)$,

$$\tau(n) = \langle\{\tau(j,k,n)\}\rangle. \quad (9)$$

We also compute residuals for each synthetic ground motion with respect to $B(i,j,k,n)$, to compute the remaining within-event variability,

$$\delta W(i,j,k,l,m,n) = ln(Y_{\text{sim}}(i,j,k,l,m,n)) - B(i,j,k,n), \quad (10)$$

which is analogous to δW_{es} in Al Atik *et al.* (2010). We take the single-site within-event standard deviation, computed at site j, for ruptures matching scenario n, and at a fixed distance k to be

$$\phi_{ss}(j,k,n) = \text{st.dev.}\{\delta W(i,j,k,l,m,n)|i \in 1..N_{\text{rup}}, \times l \in 1..N_{\text{az}}, m \in 1..N_{\text{path}}\}. \quad (11)$$

We estimate single-site within-event standard deviation computed for site j and across all distances as

$$\phi_{ss}(j,n) = \text{st.dev.}\{\delta W(i,j,k,l,m,n)|i \in 1..N_{\text{rup}}, \times k \in 1..N_{\text{dist}}, l \in 1..N_{\text{az}}, m \in 1..N_{\text{path}}\}, \quad (12)$$

across all sites for a single distance k as

$$\phi_{ss}(k,n) = \text{st.dev.}\{\delta W(i,j,k,l,m,n)|i \in 1..N_{\text{rup}}, \times j \in 1..N_{\text{site}}, l \in 1..N_{\text{az}}, m \in 1..N_{\text{path}}\}, \quad (13)$$

and for all ruptures matching scenario n as the standard deviation of all residuals for n,

$$\phi_{ss}(n) = \text{st.dev.}\{\delta W(i,j,k,l,m,n)|i \in 1..N_{\text{rup}}, j \in 1..N_{\text{site}}, \times k \in 1..N_{\text{dist}}, l \in 1..N_{\text{az}}, m \in 1..N_{\text{path}}\}. \quad (14)$$

VARIANCE DECOMPOSITION RESULTS

Table 1 summarizes computed between-event standard deviations for each scenario, $\tau(n)$, along with the range of values computed at a single site, $\tau(j,n)$, and values for each distance (computed across all sites), $\tau(k,n)$. The simulated $\tau(n)$ values are 0.18, 0.17, and 0.14 for the **M** 6.6 strike slip, **M** 6.6 reverse,

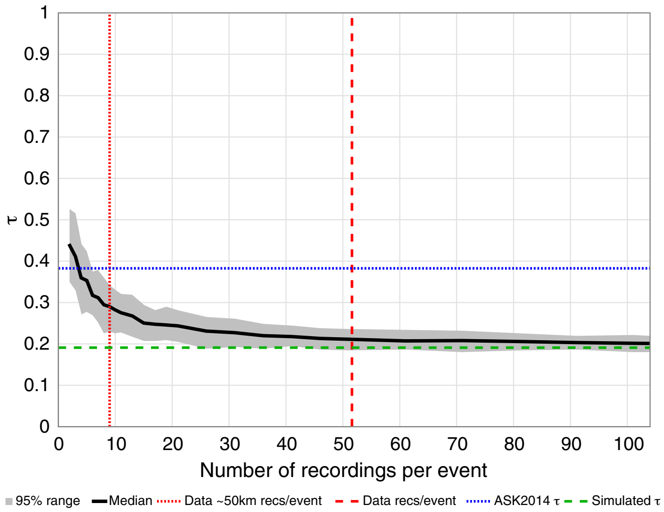

Figure 14. Simulated $\tau(k, n)$ as a function of the number of synthetic recordings per rupture ($N_{\rm rec}$) for the **M** 6.6 vertical strike-slip scenario at 50 km distance. For each $N_{\rm rec}$ value, we randomly sample $N_{\rm rec}$ simulated ground motions from the full set, from which we compute downsampled $\tau(k, n)$. We repeat this 100 times for each $N_{\rm rec}$, to estimate a distribution of downsampled $\tau(k, n)$ values, the median of which is plotted with a thick black line, and the 95% range is depicted as a light-gray shaded region. The full simulated $\tau(k, n)$ value (using all available simulations) is plotted with a horizontal dashed line, and the τ value estimated from the ASK2014 GMM is plotted with a dotted horizontal line. The average number of recordings of 3 s RotD50 SA per event for $\boldsymbol{M} \in [6.4, 6.8]$ ruptures (at any distance) in the database used in the ASK2014 regressions is indicated with a vertical dashed line, and the average number of recordings for those ruptures within a distance range of $R_{\rm Rup} \in [40, 60]$ km is indicated with a vertical dotted line. The color version of this figure is available only in the electronic edition.

and **M** 7.2 strike-slip scenarios, respectively; these are significantly lower than the values of 0.38 and 0.36 determined in the ASK2014 regressions for **M** 6.6 and **M** 7.2, respectively, indicating that the model lacks sufficient between-event variability by this metric. One potential explanation for this discrepancy is that uncertainty on δB_e in GMM regressions (e.g., due to earthquakes with few recordings per event) may artificially inflate τ. Figure 14 plots $\tau(k, n)$ computed from suites of downsampled synthetic data as a function of the number of simulated recordings per event, $N_{\rm rec}$. Here, for each $N_{\rm rec}$ value, we estimate downsampled $B(i, k, n)$ from a randomly sampled subset of $N_{\rm rec}$ ground motions for each rupture, then compute downsampled $\tau(k, n)$ following equation (8). We do this 100 times for each $N_{\rm rec}$ to compute a distribution of downsampled $\tau(k, n)$, the median of which decreases with increasing $N_{\rm rec}$ and asymptotes to the full simulated $\tau(k, n)$ value. This indicates that our modeled $\tau(k, n)$, in which $B(i, k, n)$ is well constrained by a large set of $N_{\rm site} \times N_{\rm az} \times N_{\rm path} = 3240$ simulations, should be lower than τ estimated from sparse data; however, this effect only explains part of the τ discrepancy.

Another potential explanation is that the magnitudes in the GMM may be associated with a wider range of stress drop and magnitude-area estimates than in our simulations, which come directly out of the RSQSim model. More generally, magnitudes and distances are perfectly known in our experiment, whereas those source parameters of real earthquakes are uncertain. We chose to select ruptures from the RSQSim catalogs with magnitudes in a tight range (e.g., $\boldsymbol{M} \in [7.15, 7.25]$ for the **M** 7.2 scenario), and distances are fixed by construction. These differences, along with the previously discussed recordings-per-event dependence, highlight how the paucity of data used in empirical models can inflate τ, and, thus, our simulated $\tau(n)$ cannot be considered a perfect analog to empirical τ. That said, this analysis reveals a potential lack of between-event variability that warrants consideration in the development of future RSQSim models. Table 1 also indicates that we do not see a significant dependence of $\tau(k, n)$ on distance, consistent with the empirical models.

Table 2 summarizes computed within-event standard deviations for each scenario, $\phi_{\rm ss}(n)$, along with the range of values computed at a single site, $\phi_{\rm ss}(j, n)$, and values for each distance (computed across all sites), $\phi_{\rm ss}(k, n)$. The simulated $\phi_{\rm ss}(n)$ values are 0.48, 0.44, and 0.44 for the **M** 6.6 strike slip, **M** 6.6 reverse, and **M** 7.2 strike-slip scenarios, respectively. The NGA-West2 relations do not explicitly define $\phi_{\rm ss}$, but Al Atik (2015) estimates a value of 0.37 (their table 5.11) and Lin *et al.* (2011) a value of 0.42 (their table 3, column σ_r). These estimates are both below our simulated $\phi_{\rm ss}(n)$, indicating that our model produces a sufficient amount of within-event ground-motion variability. One feature of note from Table 2 is that our $\phi_{\rm ss}(n, k)$ increases significantly with distance, which is not included in ASK2014, Lin *et al.* (2011), or Al Atik (2015). The Boore *et al.* (2014) model is the only NGA-West2 relation that includes distance dependence of ϕ, but that dependence is only for distances greater than 130 km. This distance dependence is not observed when we do the same calculation with a 1D velocity structure with the BBP, so it is likely due to increased path effects at greater distances in the 3D velocity model (tables of 1D variability results are given in the supplemental material). Those 3D path effects are velocity model and region specific, so we expect to see different amounts of distance dependence and total within-event variability with different 3D velocity models and in different regions. This regional dependence is also a possible explanation for our larger $\phi_{\rm ss}(n)$ values relative to Lin *et al.* (2011) and Al Atik (2015), which were computed for Taiwan and the central and eastern United States, respectively. In addition, $\phi_{\rm ss}(j, n)$ varies widely from site-to-site (e.g., spanning a range of [0.38, 0.64] for the **M** 6.6 strike-slip scenario), and, although, we attempted to select a diverse and representative set of sites, we expect that $\phi_{\rm ss}(n)$ is sensitive to that choice.

FULLY PHYSICS-BASED HAZARD CURVES

We compute fully nonergodic PSHA hazard curves from the suite of simulated ground motions, for the complete synthetic catalog of $N_{\rm rup} = 95{,}803$ RSQSim ruptures. This process is similar to traditional GMM-based hazard curves, except that each ith rupture has a single simulated ground-motion intensity at the jth site, $Y_{\mathrm{sim}}(i, j)$, rather than an empirically predicted lognormal distribution, and the same annual rate of occurrence, R, equal to the reciprocal of the simulated catalog duration, ΔT, expressed in years:

$$R = \Delta T^{-1}. \tag{15}$$

The number of ruptures of which simulated intensity, $Y_{\mathrm{sim}}(i, j)$, exceeds intensity measure level L at site j, modified from equation (11) of Wang and Jordan (2014) in which H is the Heaviside step function, is

$$N_{\mathrm{exceed}}(j, L) = \sum_{i=1}^{N_{\mathrm{rup}}} H[Y_{\mathrm{sim}}(i, j) - L]. \tag{16}$$

The time-independent annual probability of exceeding L at site j can then be expressed, assuming Poissonian behavior, as

$$P(Y_{\mathrm{sim}} > L|j, R) = 1 - e^{-R \times N_{\mathrm{exceed}}(j,L)}. \tag{17}$$

This results in a minimum possible nonzero probability for a single exceedance, $N_{\mathrm{exceed}} = 1$, of

$$P_{\min} = 1 - e^{-R}, \tag{18}$$

for any L. Longer simulations give more opportunities to exceed large intensity measures, and thus can probe lower probability regions, but typical hazard levels of interest (e.g., less than 10,000-yr return periods) are well resolved with our 714,516 yr RSQSim catalog. Hazard curves expressing the probability of exceeding 3 s RotD50 PSA at the USC site are shown in Figure 15a. Figure 15b illustrates the effect of simulated catalog length on $P_{\min}$ and resultant hazard curves, which differ little for return periods less than 10,000 yr (though the minimum sufficient catalog length may be much longer for areas where hazard is controlled by faults with low slip rates). At low exceedance probabilities ($<10^{-4}$), the slope of the simulated hazard curve is the most similar to truncated GMM curves (depicted with dashed and dotted lines in Fig. 15a).

The effect of decreased variability for individual source–site pairs in the nonergodic RSQSim–CyberShake model can be seen at multiple points on simulated hazard curves. Curves for the USC site, computed with the CyberShake and ASK2014 models, are both controlled by contributions from the San Andreas below 0.1g, but the tight distribution centered about 0.03g for **M** 7–7.5 events (previously observed in Fig. 9a) leads to increased exceedance probabilities in the CyberShake curve up to 0.08g. This is better illustrated through hazard curves for individual faults in Figure 16, in which each individual source curve represents the hazard only considering ruptures for which the named fault participates. Here, we can see that the San Andreas controls the hazard at higher

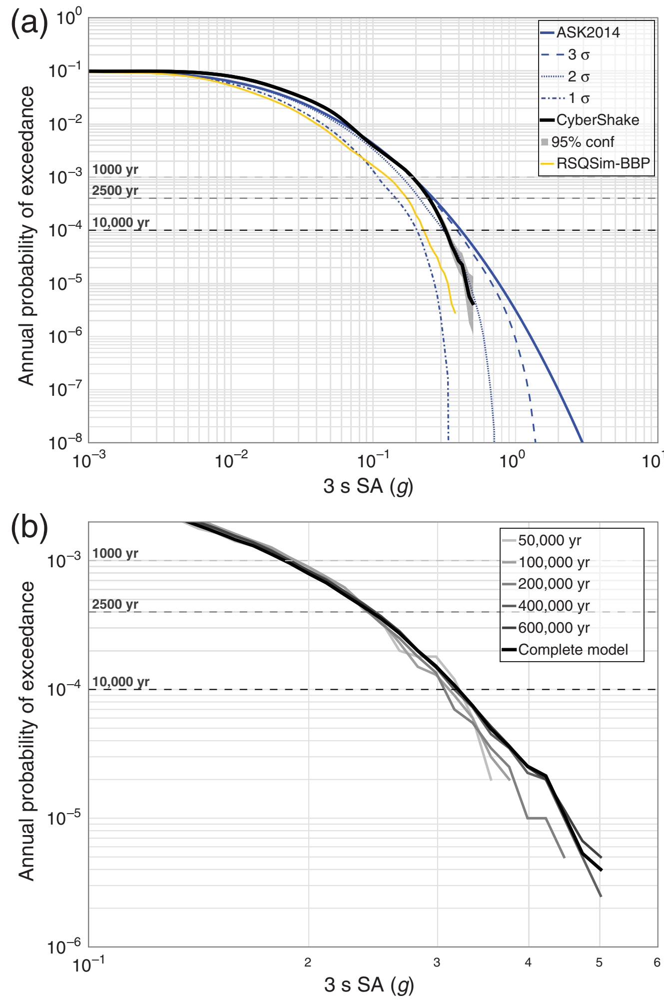

Figure 15. RSQSim simulation hazard curves at USC. CyberShake (3D) is plotted with thick, black lines. (a) ASK2014 GMM comparisons curves in blue, with the complete hazard curve plotted as a thick solid line. GMM curves computed from truncated lognormal distributions at 3-, 2-, and 1-σ are plotted with dashed, dotted, and dotted and dashed lines, respectively. The 1D BBP hazard curve is included in yellow, and 95% confidence bounds assuming a binomial distribution (representing sampling uncertainty from a finite catalog duration) on the 3D simulated curve are depicted as a gray shaded region. (b) An enlarged view of CyberShake hazard curves, including curves computed with different RSQSim catalog lengths. The complete catalog is shown (after discarding spin-up time) with a thick black line, and subsets of the catalog, starting with the first 50,000 simulated yr in light gray, are shown in thin and increasingly dark lines with increasing duration.

exceedance probabilities ($>10^{-3}$), and, the shape of the full simulated hazard curve in Figure 16 follows the shape of the San Andreas curve up to 0.08g, before transitioning to track the lower probability nearby faults that produce the largest ground motions. San Andreas controls the GMM curve up to 0.2g in Figure 16b, due to the smoother and wider exceedance distribution predicted by the ergodic model.

Similar effects can be seen at the rest of the sites, which are plotted in the supplemental material. The most extreme hazard curves are plotted in Figures 17a,b for sites SBSM and OSI,

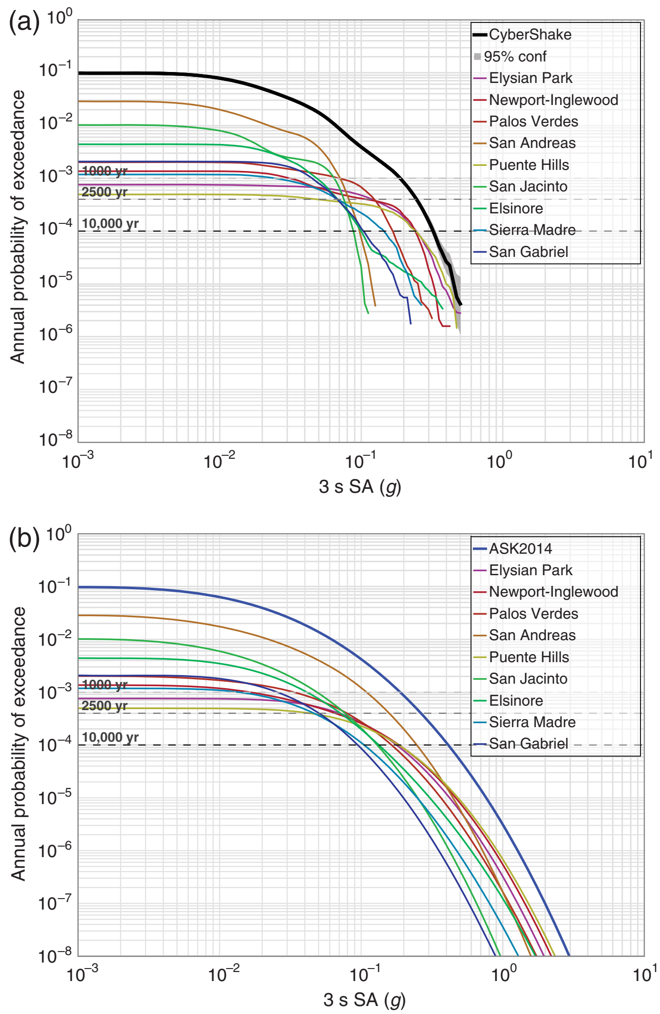

Figure 16. Source contributions for RSQSim hazard curves computed at USC. Individual fault contributions are shown with thin colored lines. (a) Results computed with CyberShake, with the total CyberShake curve on top, as a thick black line. (b) Results computed with the empirical ASK2014 GMM, with the total GMM curve on top, as a thick blue line.

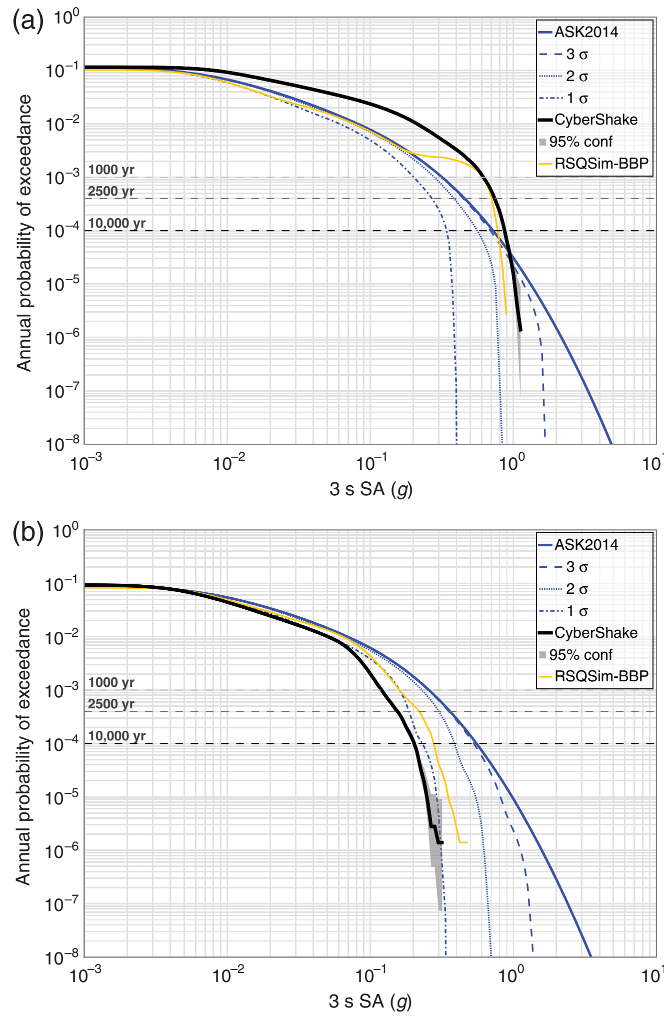

Figure 17. Same as Figure 15a, except for panel (a) site SBSM and (b) site OSI. Site locations are listed in the supplemental material and plotted in Figure 10.

respectively. Site SBSM is located on a bed of soft sediments in the San Bernardino basin, near the San Andreas fault and directly above the San Jacinto fault. Exceedance probabilities for the CyberShake hazard curve up to 0.9g are significantly larger than those from ASK2014, and the mean CyberShake z-score at this site is 1.06. Site OSI is located in a mountainous area, with just a thin layer of soft sediments overlaying high-velocity hard rock. In this case, the CyberShake hazard curve is below even the $1 - \sigma$ truncated ASK2014 curve at all ground-motion levels, and the mean CyberShake z-score is −0.31. These two sites are examples in which physics-based approaches might be able to capture details of local-site conditions, which are not well described by simple parameterizations (e.g., V_{S30} and $Z_{1.0}$) in ergodic models.

Values of risk-targeted ground motion (RTGM; Luco *et al.*, 2007), the probabilistic design level specified in the American Society of Civil Engineers 7-10 and 7-16 provisions, are listed in Table 3 for each site. There, we see that the RTGMs computed from CyberShake are lower than or equal (to two decimal points) to those from ASK2014 for seven of 10 sites. SBSM is the only site in our study with a significantly larger CyberShake RTGM, in this case 76% larger than the ASK2014 RTGM. We selected the SBSM site because previous CyberShake studies found large discrepancies between GMMs and CyberShake at this location; future RSQSim-CyberShake studies (e.g., a full regional hazard map) would likely identify other sites that also produce larger design-level ground motions.

DISCUSSION

The fully physics-based PSHA hazard curves presented in Figures 15–17 show the potential of future fully nonergodic PSHA studies. Resultant hazard curves can change dramatically when individual source and path effects are uniquely

TABLE 3
Risk-Targeted Ground Motions

Site Name	CyberShake RTGM	ASK2014 RTGM
LAF	0.19	0.24
OSI	0.15	0.32
PDE	0.24	0.25
s022	0.25	0.26
SBSM	0.72	0.41
SMCA	0.26	0.25
STNI	0.23	0.25
USC	0.23	0.24
WNGC	0.26	0.25
WSS	0.14	0.15

Risk-targeted ground motions (RTGMs; Luco *et al.*, 2007) computed from hazard curves from CyberShake (3 s spectral acceleration [SA]) and the Abrahamson *et al.* (2014; henceforth ASK2014) empirical ground-motion model (GMM) for each of the sites mapped in Figure 10 (locations listed in the supplemental material).

characterized. Individual sources, such as the San Andreas fault in the Los Angeles region, can produce characteristic ground motions with significantly less variability than predicted in ergodic GMMs. The slope at low probabilities may also be much steeper for nonergodic curves; empirical GMMs extend to infinite ground motion at infinitely low probability, but simulation curves are bound by a minimum possible probability, $P_{\min}$, at the level of the largest simulated ground motion. Here, simulated curves appear more similar to GMM curves computed with truncated distributions above $P_{\min}$. Even though CyberShake ground motions in this study are larger on average than those from ASK2014 (Fig. 11b), design-level ground motions (Table 3) for the CyberShake model are lower than or equal to those from ASK2014 at a majority of sites. This reduction is precisely the goal of nonergodic PSHA: to characterize sites most likely to experience higher than average ground motions due to local site or path effects (e.g., at site SBSM in this model), without extending that higher hazard to all sites uniformly.

Although consistency of mean ground-motion predictions in simulation-based PSHA with data and empirical models is important, ground-motion variability typically controls hazard at levels of engineering interest (Anderson and Brune, 1999). A viable nonergodic PSHA model should contain similar total variability to ergodic models, after sampling a sufficiently diverse set of sites and sources. We outlined a method for evaluating the total variability of such a model through z-score histograms, which indicate that the RSQSim–CyberShake model has a comparable amount of total variability as empirical models. This is a necessary validation step, but it is not sufficient, as the individual components of variability, both between and within events, are well studied in the literature and constrained with data. We outlined a method to estimate these components through rotation and translation of ruptures about various sites in a 3D medium. Calculated within-event variability estimates indicate that the RSQSim model, at present, produces ruptures that are sufficiently heterogeneous to produce realistic ground-motion fields at $T = 3$ s. These calculations also revealed a potential deficit of between-event variability, which will be a focus of future RSQSim–CyberShake studies, as well as possible inflation of empirically estimated between-event variability due to data uncertainties.

A benefit to the use of RSQSim ruptures directly in CyberShake is the presence of multifault ruptures, which are a key component of the UCERF3 model. Even though UCERF3 was first released in 2013, CyberShake (with the exception of this study) still employs the prior UCERF2 model. This is largely due to limitations with the current kinematic rupture generator, which has not yet been configured to simulate complex multifault ruptures (such as the one depicted in Fig. 5) in a fully automatic fashion to account for moment partitioning and timing. If CyberShake is to continue to rely on empirical ERFs, then as they increase in complexity, so must the rupture generators to accommodate more complex geometries. At some point, it becomes simpler to use a simulated extended ERF like RSQSim directly, which eliminates the kinematic rupture generator entirely, though that approach comes with its own set of uncertainties. The similarity of RSQSim to UCERF3 observed by Shaw *et al.* (2018) indicates that an RSQSim-derived ERF could be used by CyberShake to capture some of the UCERF3 improvements over UCERF2, without the computational challenges. We are focused on calibrating the model in California, a region for which we have well-characterized earthquake sources and a relatively well populated ground-motion dataset. However, because RSQSim is based on defensible seismological and physical processes, we expect that the calibrated version will be portable to other tectonic regions as well.

Extensive validation, model development, and inclusion of epistemic uncertainties are required before fully physics-based PSHA can replace current ergodic approaches. This study illustrates initial results and validations for a single RSQSim model, whereas a robust hazard estimate must characterize its uncertainties. Shaw (2006) found that rupture nucleation, termination, and propagation in multicycle earthquake simulations are highly sensitive to fault geometries (including endpoints, connecting structures, and geometric complexities), which are poorly constrained at seismogenic depths. This sensitivity manifests as nucleation hotspots in our model, which further reduce ground-motion variability for some individual source–site pairs due to repeated rupture directivity. In addition (and as with prior UCERF2-based CyberShake studies), characterization of ground-motion path effects is highly dependent on the underlying velocity model, which is uncertain; these sensitivities require further study and should be represented as epistemic uncertainties. Finally, inclusion of uncertainties (including spatial variability) in frictional parameters might help with the deficit of between-event variability noted, by sampling a wider range of stress drops.

An ideal physics-based PSHA model would include fully dynamic multicycle (e.g., thousands to millions of years of seismicity) simulation of rupture nucleation and resultant ground motions in a realistic 3D nonlinear medium, but such a calculation on a large simulation domain with a complex fault system is intractable on even the largest supercomputers. Although Richards-Dinger and Dieterich (2012) found that RSQSim compares favorably to fully dynamic models, it includes quasistatic approximations in the name of computational efficiency, which warrant further sensitivity analysis and comparison with other competing models with different assumptions. Even if the underlying models were thoroughly validated, current computational methods are intractable at high frequencies (e.g., 10 Hz) for large ensembles of ruptures required for PSHA, as higher frequencies require consideration of nonlinearities. Still, as models evolve and computing power increases, these deficiencies can be addressed and epistemic uncertainties reduced. Until then, simulation-based PSHA models like RSQSim–CyberShake might inform hybrid models that combine empirical datasets (or ergodic GMMs) with nonergodic source, path, and site effects from simulations; further exploration of the RSQSim–CyberShake model (e.g., a hazard map for the Los Angeles region) is warranted.

DATA AND RESOURCES

All simulated Rate-State earthquake simulator (RSQSim)–CyberShake 3 s ground-motion intensities used in this study are included in the supplemental material. Hazard and empirical ground-motion model (GMM) calculations were performed with the OpenSHA platform, available at https://github.com/opensha (last accessed June 2020). The Southern California Earthquake Center (SCEC) Broadband Platform is available at https://github.com/SCECcode/bbp (last accessed June 2020). Plots were made with JFreeChart (http://www.jfree.org/jfreechart/, last accessed June 2020) and the Generic Mapping Tools (https://www.generic-mapping-tools.org/, last accessed June 2020). More information on CyberShake Study 15.4 is available at https://strike.scec.org/scecpedia/CyberShake_Study_15.4 (last accessed December 2020). The Standard Rupture Format is described at http://equake-rc.info/static/paper/SRF-Description-Graves_2.0.pdf (last accessed December 2019). Any use of trade, firm, or product names is for descriptive purposes only and does not imply endorsement by the U.S. Government.

ACKNOWLEDGMENTS

Work here was performed within the Collaboratory for Interseismic Simulation and Modeling (CISM) through a Grant from the W. M. Keck Foundation. This research was also supported by the Southern California Earthquake Center (SCEC); the SCEC Contribution Number for this article is 10107. SCEC is funded by U.S. Geological Survey Cooperative Agreement G17AC00047 and National Science Foundation (NSF) Cooperative Agreement EAR-1600087. SCEC Broadband Platform (BBP) calculations were performed at the University of Southern California Center for high-performance computing and communications. Rate-State earthquake simulator (RSQSim) catalogs were generated on the Frontera supercomputer at Texas Advanced Computing Center (TACC) at The University of Texas at Austin, and the Blue Waters sustained-petascale computing project, which is supported by the NSF (Awards OCI-0725070 and ACI-1238993) and the State of Illinois. Blue Waters is a joint effort of the University of Illinois at Urbana–Champaign and its National Center for Supercomputing Applications. This work is also supported by a Leadership-Class Computing Resource Allocations (PRAC) allocation supported by NSF (Award Number OAC-1713792). RSQSim–CyberShake ground-motion calculations were performed at the Oak Ridge Leadership Computing Facility, which is a Department of Energy Office of Science User Facility supported under Contract DE-AC05-00OR22725. This material is based upon work supported by the U.S. Geological Survey under Grant Number G19AP00081. The authors thank Jacquelyn Gilchrist for her significant contributions to CISM, Philip Maechling for his leadership of SCEC computational science activities, Fabio Silva for his excellent documentation and help integrating RSQSim ruptures with the SCEC BBP, Robert Graves for his valuable feedback and clear explanations, and three anonymous reviewers whose incredibly detailed and constructive feedback improved this article greatly. The views and conclusions contained in this article are those of the authors and should not be interpreted as representing the opinions or policies of the U.S. Geological Survey.

REFERENCES

Abrahamson, N. A., W. J. Silva, and R. Kamai (2014). Summary of the ASK14 ground motion relation for active crustal regions, *Earthq. Spectra* **30,** no. 3, 1025–1055, doi: 10.1193/070913EQS198M.

Abrahamson, N. A., and R. R. Youngs (1992). A stable algorithm for regression analyses using the random effects model, *Bull. Seismol. Soc. Am.* **82,** no. 1, 505–510.

Aki, K., and P. G. Richards (2009). *Quantitative Seismology*, Second Ed., University Science Books, Sausalito, California.

Al Atik, L. (2015). *NGA-East: Ground-motion standard deviation models for central and eastern North America*, *PEER Rept. 2015-07*, Berkeley, California.

Al Atik, L., N. Abrahamson, J. J. Bommer, F. Scherbaum, F. Cotton, and N. Kuehn (2010). The variability of ground-motion prediction models and its components, *Seismol. Res. Lett.* **81,** no. 5, 794–801, doi: 10.1785/gssrl.81.5.794.

Al Atik, L., and N. A. Abrahamson (2010). Nonlinear site response effects on the standard deviations of predicted ground motions, *Bull. Seismol. Soc. Am.* **100,** no. 3, 1288–1292, doi: 10.1785/0120090154.

Anderson, J. G., and J. N. Brune (1999). Probabilistic seismic hazard analysis without the ergodic assumption, *Seismol. Res. Lett.* **70,** no. 1, 19–28.

Andrews, D. J. (1976). Rupture velocity of plane strain shear cracks, *J. Geophys. Res.* **81,** no. 32, 5679–5687.

Boore, D. M. (2010). Orientation-independent, nongeometric-mean measures of seismic intensity from two horizontal components of motion, *Bull. Seismol. Soc. Am.* **100,** no. 4, 1830–1835, doi: 10.1785/0120090400.

Boore, D. M., J. P. Stewart, E. Seyhan, and G. M. Atkinson (2014). NGA-West2 equations for predicting PGA, PGV, and 5% damped PSA for shallow crustal earthquakes, *Earthq. Spectra* **30,** no. 3, 1057–1085, doi: 10.1193/070113EQS184M.

Bozorgnia, Y., N. A. Abrahamson, L. A. Atik, T. D. Ancheta, G. M. Atkinson, J. W. Baker, A. Baltay, D. M. Boore, M. Campbell, B. S. J. Chiou, *et al.* (2014). NGA-West2 research project, *Earthq. Spectra* **30,** no. 3, 973–987, doi: 10.1193/072113EQS209M.

Brune, J. N. (1970). Tectonic stress and the spectra of seismic shear waves from earthquakes, *J. Geophys. Res.* **75,** no. 26, 4997–5009, doi: 10.1029/JB075i026p04997.

Campbell, K. W., and Y. Bozorgnia (2014). NGA-West2 ground motion model for the average horizontal components of PGA, PGV, and 5% damped linear acceleration response spectra, *Earthq. Spectra* **30,** no. 3, 1087–1115, doi: 10.1193/062913EQS175M.

Chiou, B. S. J., and R. R. Youngs (2014). Update of the Chiou and Youngs NGA model for the average horizontal component of peak ground motion and response spectra, *Earthq. Spectra* **30,** no. 3, 1117–1153, doi: 10.1193/072813EQS219M.

Cornell, C. A. (1968). Engineering seismic risk analysis, *Bull. Seismol. Soc. Am.* **58,** no. 5, 1583–1606.

Cui, Y., E. Poyraz, J. Zhou, S. Callaghan, P. Maechling, T. H. Jordan, L. Shih, and P. Chen (2013). Accelerating CyberShake calculations on the XE6/XK7 platform of Blue Waters, *2013 Extreme Scaling Workshop (XSW 2013)*, Boulder, Colorado, 8–17, doi: 10.1109/XSW.2013.6.

Dieterich, J. H. (1992). Earthquake nucleation on faults with rate-and state-dependent strength, *Tectonophysics* **211,** nos. 1/4, 115–134, doi: 10.1016/0040-1951(92)90055-B.

Dieterich, J. H., and K. B. Richards-Dinger (2010). Earthquake recurrence in simulated fault systems, *Pure Appl. Geophys.* **167,** 1087–1104, doi: 10.1007/s00024-010-0094-0.

Field, E. H., R. J. Arrowsmith, G. P. Biasi, P. Bird, T. E. Dawson, K. R. Felzer, D. D. Jackson, K. M. Johnson, T. H. Jordan, C. Madden, *et al.* (2014). Uniform California Earthquake Rupture Forecast, version 3 (UCERF3)—The time-independent model, *Bull. Seismol. Soc. Am.* **104,** no. 3, 1122–1180, doi: 10.3133/ofr20131165.

Field, E. H., T. E. Dawson, K. R. Felzer, A. D. Frankel, V. Gupta, T. H. Jordan, T. Parsons, M. D. Petersen, R. S. Stein, R. J. Weldon, and C. J. Wills (2009). Uniform California Earthquake Rupture Forecast, version 2 (UCERF 2), *Bull. Seismol. Soc. Am.* **99,** no. 4, 2053–2107, doi: 10.1785/0120080049.

Galvez, P., P. Somerville, A. Petukhin, J. P. Ampuero, and D. Peter (2019). Earthquake cycle modelling of multi-segmented faults: Dynamic rupture and ground motion simulation of the 1992 M_w 7.3 Landers earthquake, *Pure Appl. Geophys.* **177,** 2163–2179, doi: 10.1007/s00024-019-02228-x.

Geller, R. J. (1976). Scaling relations for earthquake source parameters and magnitudes, *Bull. Seismol. Soc. Am.* **66,** no. 5, 1501–1523.

Goulet, C. A., N. A. Abrahamson, P. G. Somerville, and K. E. Wooddell (2014). The SCEC Broadband Platform validation exercise: Methodology for code validation in the context of seismic-hazard analyses, *Seismol. Res. Lett.* **86,** no. 1, 17–26, doi: 10.1785/0220140104.

Graves, R., T. H. Jordan, S. Callaghan, E. Deelman, E. Field, G. Juve, C. Kesselman, P. Maechling, G. Mehta, K. Milner, *et al.* (2011). CyberShake: A physics-based seismic hazard model for southern California, *Pure Appl. Geophys.* **168,** nos. 3/4, 367–381, doi: 10.1007/s00024-010-0161-6.

Graves, R., and A. Pitarka (2014). Refinements to the Graves and Pitarka (2010) broadband ground-motion simulation method, *Seismol. Res. Lett.* **86,** no. 1, 75–80, doi: 10.1785/0220140101.

Graves, R., and A. Pitarka (2016). Kinematic ground-motion simulations on rough faults including effects of 3D stochastic velocity perturbations, *Bull. Seismol. Soc. Am.* **106,** no. 5, 2136–2153, doi: 10.1785/0120160088.

Jordan, T. H., S. Callaghan, R. W. Graves, F. Wang, K. R. Milner, C. A. Goulet, P. J. Maechling, K. B. Olsen, Y. Cui, G. Juve, *et al.* (2018). CyberShake models of seismic hazards in southern and central California, *Proc. of the 11th National Conf. in Earthquake Engineering*, Earthquake Engineering Research Institute, Los Angeles, California, 25–29 June.

Lee, E. J., P. Chen, T. H. Jordan, P. B. Maechling, M. A. Denolle, and G. C. Beroza (2014). Full-3-D tomography for crustal structure in southern California based on the scattering-integral and the adjoint-wavefield methods, *J. Geophys. Res.* **119,** no. 8, 6421–6451, doi: 10.1002/2014JB011346.

Lin, P. S., B. Chiou, N. Abrahamson, M. Walling, C. T. Lee, and C. T. Cheng (2011). Repeatable source, site, and path effects on the standard deviation for empirical ground-motion prediction models, *Bull. Seismol. Soc. Am.* **101,** no. 5, 2281–2295, doi: 10.1785/0120090312.

Luco, N., B. R. Ellingwood, R. O. Hamburger, J. D. Hooper, J. K. Kimball, and C. A. Kircher (2007). Risk-targeted versus current seismic design maps for the conterminous United States, *SEAOC 2007 Convention Proc. Structural Engineers Association of California*, Lake Tahoe, California, 26–29 September.

Maechling, P. J., F. Silva, S. Callaghan, and T. H. Jordan (2014). SCEC Broadband Platform: System architecture and software implementation, *Seismol. Res. Lett.* **86,** no. 1, 27–38, doi: 10.1785/0220140125.

Richards-Dinger, K., and J. H. Dieterich (2012). RSQSim earthquake simulator, *Seismol. Res. Lett.* **83,** no. 6, 983–990, doi: 10.1785/0220120105.

Shaw, B. E. (2006). Initiation propagation and termination of elastodynamic ruptures associated with segmentation of faults and shaking hazard, *J. Geophys. Res.* **111,** no. B08302, doi: 10.1029/2005JB004093.

Shaw, B. E. (2019). Beyond backslip: Improvement of earthquake simulators from new hybrid loading conditions, *Bull. Seismol. Soc. Am.* **109,** no. 6, 2159–2167, doi: 10.1785/0120180128.

Shaw, B. E., K. R. Milner, E. H. Field, K. Richards-Dinger, J. J. Gilchrist, J. H. Dieterich, and T. H. Jordan (2018). A physics-based earthquake simulator replicates seismic hazard statistics across California, *Sci. Adv.* **4,** no. 8, eaau0688, doi: 10.1126/sciadv.aau0688.

Small, P., D. M. Gill, P. J. Maechling, R. Taborda, S. Callaghan, T. H. Jordan, K. B. Olsen, G. P. Ely, and C. A. Goulet (2017). The SCEC unified community velocity model software framework, *Seismol. Res. Lett.* **88,** no. 6, 1539–1552, doi: 10.1785/0220170082.

Wang, F., and T. H. Jordan (2014). Comparison of probabilistic seismic-hazard models using averaging-based factorization, *Bull. Seismol. Soc. Am.* **104,** no. 3, 1230–1257.

Zhao, L., P. Chen, and T. H. Jordan (2006). Strain Green's tensors, reciprocity, and their applications to seismic source and structure studies, *Bull. Seismol. Soc. Am.* **96,** no. 5, 1753–1763, doi: 10.1785/0120050253.

Manuscript received 22 June 2020
Published online 05 January 2021